

Field-induced SU(4) to SU(2) Kondo crossover in a half-filling nanotube dot: Spectral and finite-temperature properties

Yoshimichi Teratani ¹, Rui Sakano,² Tokuro Hata,³ Tomonori Arakawa,^{3,4}
Meydi Ferrier,^{3,5} Kensuke Kobayashi ^{3,6} and Akira Oguri^{1,7}

¹*Department of Physics, Osaka City University, Sumiyoshi-ku, Osaka, 558-8585, Japan*

²*The Institute for Solid State Physics, the University of Tokyo, Kashiwa, Chiba 277-8581, Japan*

³*Department of Physics, Osaka University, Toyonaka, Osaka 560-0043, Japan*

⁴*Center for Spintronics Research Network, Osaka University, Toyonaka, Osaka 560-8531, Japan*

⁵*Laboratoire de Physique des Solides, CNRS, Université Paris-Sud, Université Paris Saclay, 91405 Orsay Cedex, France*

⁶*Institute for Physics of Intelligence and Department of Physics, The University of Tokyo, Tokyo 113-0033, Japan*

⁷*Nambu Yoichiro Institute of Theoretical and Experimental Physics, Sumiyoshi-ku, Osaka, 558-8585, Japan*



(Received 29 March 2020; revised 17 September 2020; accepted 18 September 2020; published 6 October 2020)

We study finite-temperature properties of the Kondo effect in a carbon nanotube (CNT) quantum dot using the Wilson numerical renormalization group (NRG). In the absence of magnetic fields, four degenerate energy levels of the CNT consisting of spin and orbital degrees of freedom give rise to the SU(4) Kondo effect. We revisit the universal scaling behavior of the SU(4) conductance for quarter- and half-filling in a wide temperature range. We find that the filling dependence of the universal scaling behavior at low temperatures T can be explained clearly with an extended Fermi-liquid theory. This theory clarifies that a T^2 coefficient of conductance becomes zero at quarter-filling, whereas the coefficient at half-filling is finite. We also study a field-induced crossover from the SU(4) to SU(2) Kondo state observed at the half-filled CNT dot. The crossover is caused by the matching of the spin and orbital Zeeman splittings, which lock two levels among the four at the Fermi level even in magnetic fields B . We find that the conductance shows the SU(4) scaling behavior at $\mu_B B < k_B T_K^{\text{SU}(4)}$ and it exhibits the SU(2) universality at $\mu_B B \gg k_B T_K^{\text{SU}(4)}$, where $T_K^{\text{SU}(4)}$ is the SU(4) Kondo temperature. To clarify how the excited states evolve along the SU(4) to SU(2) crossover, we also calculate the spectral function. The results show that the Kondo resonance width of the two states locked at the Fermi level becomes sharper with increasing fields. The spectral peaks of the other two levels moving away from the Fermi level merge with atomic limit peaks for $\mu_B B \gtrsim k_B T_K^{\text{SU}(4)}$.

DOI: [10.1103/PhysRevB.102.165106](https://doi.org/10.1103/PhysRevB.102.165106)

I. INTRODUCTION

Quantum dots provide an ideal testbed to investigate strong correlations between the electrons in localized levels and the conduction electrons in reservoirs. Kondo effect [1,2] is a typical many-body phenomenon that occurs also in quantum dots having local spin degrees of freedom. The Kondo effect in quantum dots has been studied theoretically [3,4] and experimentally [5,6]. In addition to the spin degrees of freedom, carbon nanotube (CNT) quantum dots have also the orbital (valley) degrees of freedom, corresponding to clockwise and counter clockwise orbitals around the nanotube axis [7]. Four energy levels consisting of the spin and orbital degrees of freedom give rise to the SU(4) Kondo effect in the case where the four localized states are degenerate [8–14]. A number of experiments for nonequilibrium transport have observed the SU(4) Kondo effect [15–20]. Perturbations such as spin-orbit coupling Δ_{SO} , valley mixing $\Delta_{K,K'}$ and magnetic fields B break the SU(4) symmetry. Effects of such perturbations on the Kondo state are theoretically studied for instance, using Wilson's numerical renormalization group (NRG) approach [21–23], which has been extended to explore transport

coefficients and spectral functions with very high accuracy [12,24–26].

The main purpose of the present paper is to clarify the finite temperature properties of the Kondo effect in CNT dots. In the first half of this paper, we study the scaling behavior of the SU(4) conductance at quarter- and half-filling. Although the scaling behavior has been studied [12,16,27–29], we revisit it with an extended microscopic Fermi-liquid theory which describes transport phenomena at low temperatures [30–34]. It has recently been shown that the T^2 coefficient C_T for the conductance is determined in terms of five Fermi-liquid parameters: electron filling, two linear susceptibilities, and two nonlinear susceptibilities which are defined with respect to the equilibrium ground state. Calculating these parameters using the NRG, we successfully explain the filling dependence of the scaling with the description. Specifically, we explore the filling dependence of a T^2 coefficient C_T and find that C_T becomes zero at quarter-filling whereas it is finite at half-filling.

In the second half of this paper, we examine a field induced crossover from SU(4) to SU(2) Kondo state at half-filling nanotube dot [35,36]. At the valley where the crossover

occurs, the SU(4) Kondo resonance emerges in the absence of magnetic field, because $\Delta_{K,K'}$ and Δ_{SO} are smaller than the SU(4) Kondo energy scale, $k_B T_K^{\text{SU}(4)}$. The field induced crossover is different from the other crossover occurring at quarter-filling [27,28,37–43]. Specifically, this crossover at half-filling occurs in a situation where two localized levels among the four remain the Fermi level even in magnetic fields while the other two levels move away from the Fermi level. The situation realizes if the spin Zeeman splitting coincides the orbital splitting. Such coincidence can reasonably occur in real CNT dots.

In the previous work, we have studied the crossover occurring in this situation, by calculating quasiparticle parameters such as phase shift δ , wave function renormalization factor Z and Wilson ratio R [36]. We have found that the applied magnetic fields enhance the electron correlations. For instance, as magnetic fields increase, the renormalization factor Z decreases from the SU(4) value to the SU(2) value and thus the Kondo energy scale T_K decreases. Our NRG results are in good agreement with the experimental observations [35].

In this paper, we calculate the temperature dependence of the conductance in magnetic fields to clarify the crossover in a wide range of temperature T . We show that a temperature scale T^* around which the conductance shows $\log T$ dependence decreases with increasing magnetic fields. This decrease of T^* becomes clearer in a strong Coulomb interaction case and agree with the field dependence of Z . We also examine the scaling behavior of the conductance. Whereas the conductance follows the SU(4) scaling at $\mu_B B < k_B T_K^{\text{SU}(4)}$, it shows the SU(2) scaling at $\mu_B B \gg k_B T_K^{\text{SU}(4)}$.

In addition to the conductance, we calculate the level resolved spectral functions in magnetic fields. The component for the doubly degenerate levels shows that the Kondo resonance width becomes sharper with increasing magnetic fields. This field dependence of the width corresponds to that of T^* . Spectral weights of the other two states transfer from the Fermi level, and the peaks merge with atomic limit peaks.

This paper is organized as follows. In the next section, we describe the microscopic Fermi-liquid theory and the NRG approach to CNT dots. In Sec. III, we examine the scaling behavior of the SU(4) conductance at quarter- and half-filling. We discuss how the quasiparticle parameters evolve during the field induced crossover in Sec. IV. We present the NRG results of conductance and discuss the influence of magnetic fields on the temperature dependence of conductance in Sec. V. The spectral functions in increasing magnetic fields are shown in Sec. VI. Summary is given in Sec. VII.

II. FORMULATION

Transport properties of carbon nanotube quantum dots are determined by a linear combination of four one-particle levels, consisting of the spin (\uparrow, \downarrow) and valley (K, K') degrees of freedom. The structure of these four states staying near the Fermi level depend on the inter-valley scattering, the spin-orbit coupling, and the Zeeman splittings of the spin and orbital degrees of freedom. We introduce the Anderson model for the CNT dot in this section using a diagonal form for these local levels. We provide a more microscopic description specific to a real CNT dot, in which experiments have

measured the current and corresponding noise with high accuracy. The renormalized parameters that characterize the low-energy Fermi-liquid properties and details of the NRG calculations are also described in this section.

A. Anderson model for CNT quantum dots

We start with an Anderson impurity model for a CNT dot, which has $N = 4$ internal degrees of freedom and is connected to two noninteracting leads:

$$\mathcal{H} = \mathcal{H}_d^0 + \mathcal{H}_U + \mathcal{H}_c + \mathcal{H}_T, \quad (1)$$

$$\mathcal{H}_d^0 = \sum_{m=1}^N \epsilon_m d_m^\dagger d_m, \quad \mathcal{H}_U = U \sum_{m < m'} n_{dm} n_{dm'}, \quad (2)$$

$$\mathcal{H}_c = \sum_{\nu=L,R} \sum_{m=1}^N \int_{-D}^D d\varepsilon \varepsilon c_{\nu,\varepsilon m}^\dagger c_{\nu,\varepsilon m}, \quad (3)$$

$$\mathcal{H}_T = \sum_{\nu=L,R} \sum_{m=1}^N v_\nu (\psi_{\nu,m}^\dagger d_m + d_m^\dagger \psi_{\nu,m}), \quad (4)$$

$$\psi_{\nu,m} \equiv \int_{-D}^D d\varepsilon \sqrt{\rho_c} c_{\nu,\varepsilon m}, \quad n_{dm} \equiv d_m^\dagger d_m. \quad (5)$$

Here, d_m^\dagger and d_m are the creation and annihilation operators, respectively, for an electron with energy ε_m in the m th discrete one-particle eigenstate of the dot ($m = 1, 2, \dots, N$). We shall also call m the “flavour” in the following. The Coulomb interactions U between the electrons occupying the dot levels are assumed to be independent of m , assuming that the intra- and intervalley Coulomb repulsions to be identical. We also assume that Hund’s rule coupling can be neglected. This is consistent with the CNT dot in which the field-induced SU(4) to SU(2) Kondo crossover has been observed [19], and also with the other nanotube dots [15]. \mathcal{H}_c describes conduction bands in the leads on the left and right. $\nu = L$ and $\nu = R$ respectively denote the left and right leads. The conduction electrons are assumed to carry the flavour index m , and the continuous energy states in the bands are normalized such that $\{c_{\nu,\varepsilon m}, c_{\nu',\varepsilon' m'}^\dagger\} = \delta(\varepsilon - \varepsilon') \delta_{\nu\nu'} \delta_{mm'}$. The Fermi level is chosen to be $\varepsilon_F = 0$, at the center of the flat conduction bands with the width $2D$. \mathcal{H}_T describes charge transfer between the dot and leads. We assume that the tunneling matrix element v_ν is independent of flavour m , which can also be justified for a class of CNT dots [19,35]. In this situation, the resonance width due to these hybridizations becomes $\Delta = \Delta_L + \Delta_R$ with $\Delta_\nu \equiv \pi \rho_c v_\nu^2$, and $\rho_c = 1/2D$ the density of states of the conduction band. Unless otherwise stated, we set the Boltzmann constant k_B to unity, i.e., $k_B = 1$.

This Hamiltonian \mathcal{H} has the SU(N) symmetry when all the impurity energies are equal $\epsilon_m \equiv \epsilon_d$. This is because \mathcal{H}_T that describes charge transfer preserves the flavour index m , and the Coulomb interaction is determined essentially by the total number of impurities electrons $\hat{N}_d \equiv \sum_m n_{dm}$ as $\mathcal{H}_U = (U/2) \hat{N}_d (\hat{N}_d - 1)$. In Appendix A, we explain the symmetry of this Hamiltonian in more detail.

B. Fermi-liquid parameters

The equilibrium retarded Green $G_m^r(\omega)$ is an useful tool to study transport coefficients of quantum dots. $G_m^r(\omega)$ is given by

$$G_m^r(\omega, T) \equiv -i \int_0^\infty dt e^{i(\omega+i0^+)t} \langle \{d_m(t), d_m^\dagger(0)\} \rangle \quad (6)$$

$$= \frac{1}{\omega - \epsilon_m + i\Delta - \Sigma_m(\omega, T)}, \quad (7)$$

$$A_m(\omega, T) \equiv -\frac{1}{\pi} \text{Im} G_m^r(\omega, T). \quad (8)$$

Here, $\langle \mathcal{O} \rangle \equiv \text{Tr}[\mathcal{O} e^{-\mathcal{H}/T}] / \Xi$ with $\Xi \equiv \text{Tr} e^{-\mathcal{H}/T}$ is the thermal average of an observable \mathcal{O} .

The phase shift δ_m is a primary parameter that characterizes the Fermi-liquid ground state. It is determined by the value of the self-energy $\Sigma_m(\omega, T)$ at $\omega = T = 0$,

$$\delta_m = \frac{\pi}{2} - \tan^{-1} \left[\frac{\epsilon_m + \Sigma_m(0, 0)}{\Delta} \right]. \quad (9)$$

The Friedel sum rule also relates the phase shift δ_m to the occupation number $\langle n_{dm} \rangle$ [44],

$$\langle n_{dm} \rangle = \frac{\partial \Omega}{\partial \epsilon_m} \xrightarrow{T \rightarrow 0} \frac{\delta_m}{\pi}. \quad (10)$$

Here, $\Omega = -T \ln e^{-\mathcal{H}/T}$ is the free energy. The phase shift also determines the value of the spectral function at $\omega = T = 0$,

$$A_m(0, 0) = \frac{\sin^2 \delta_m}{\pi \Delta}. \quad (11)$$

The linear susceptibilities χ_{m_1, m_2} are also important parameters that determine the Fermi-liquid properties:

$$\chi_{m_1, m_2} \equiv \int_0^{1/T} d\tau \langle \delta n_{dm_1}(\tau) \delta n_{dm_2} \rangle. \quad (12)$$

Here, $\delta n_{dm} \equiv n_{dm} - \langle n_{dm} \rangle$ is the fluctuation of the occupation number, and $\delta n_{dm}(\tau) = e^{\tau \mathcal{H}} \delta n_{dm} e^{-\tau \mathcal{H}}$. The derivative of the self-energy with respect to the impurity level also gives the susceptibilities,

$$\chi_{m_1, m_2} = -\frac{\partial^2 \Omega}{\partial \epsilon_{m_1} \partial \epsilon_{m_2}} = -\frac{\partial \langle n_{dm_1} \rangle}{\partial \epsilon_{m_2}} \xrightarrow{T \rightarrow 0} A_{m_1}(0, 0) \left(\delta_{m_1, m_2} + \frac{\partial \Sigma_{m_1}(0, 0)}{\partial \epsilon_{m_2}} \right). \quad (13)$$

The Ward-Takahashi identities relate the linear susceptibilities to the wave function renormalization factor Z_m and the vertex function $\Gamma_{mm':m'm}(0, 0; 0, 0)$ [45,46],

$$\chi_{m, m} = \frac{A_m(0, 0)}{Z_m}, \quad \frac{1}{Z_m} \equiv 1 - \left. \frac{\partial \Sigma_m(\omega, 0)}{\partial \omega} \right|_{\omega=0}, \quad (14)$$

$$\chi_{m, m'} = -A_m(0, 0) A_{m'}(0, 0) \Gamma_{mm':m'm}(0, 0; 0, 0). \quad (15)$$

$\Gamma_{mm':m'm}(\omega, \omega'; \omega', \omega)$ is the $m \neq m'$ component of the vertex correction, defined at $T = 0$ for the causal Green's functions. Note that the intra-level components for $m = m'$ vanish at zero frequencies, $\Gamma_{mm:mm}(0, 0; 0, 0) = 0$, because of the fermionic antisymmetrical properties, i.e., the Pauli exclusion principle.

The renormalized level position $\tilde{\epsilon}_m$ and corresponding resonance width $\tilde{\Delta}_m$ are determined by Z_m ,

$$\tilde{\epsilon}_m \equiv Z_m [\epsilon_m + \Sigma_m(0)], \quad \tilde{\Delta}_m \equiv Z_m \Delta. \quad (16)$$

The residual interaction between quasiparticles $\tilde{U}_{m, m'}$ is also an essential Fermi-liquid parameter [47]:

$$\tilde{U}_{m, m'} \equiv Z_m Z_{m'} \Gamma_{mm':m'm}(0, 0; 0, 0). \quad (17)$$

The Wilson ratio $R_{m, m'}$ corresponds to a dimensionless residual interaction [48], and it generally depends on m and m' :

$$R_{m, m'} \equiv 1 + \sqrt{\tilde{A}_m \tilde{A}_{m'}} \tilde{U}_{m, m'}. \quad (18)$$

Here, $\tilde{A}_m \equiv A_m(0, 0)/Z_m$ is the density of states of the quasiparticles. Using Eqs. (14)–(17), $R_{m, m'}$ can also be expressed in terms of the linear susceptibilities,

$$R_{m, m'} - 1 = -\frac{\chi_{m, m'}}{\sqrt{\chi_{m, m} \chi_{m', m'}}}. \quad (19)$$

we calculate the renormalization factor Z_m and residual interaction $\tilde{U}_{m, m'}$ using the NRG, and deduce the Wilson ratio $R_{m, m'}$ from Eq. (18). We note that the linear susceptibility $\chi_{m, m}$ determines the T -linear specific heat \mathcal{C}_{dot} due to the impurity,

$$\mathcal{C}_{\text{dot}} = \gamma T, \quad \gamma = \frac{\pi^2}{3} \sum_m \chi_{m, m}. \quad (20)$$

Furthermore, fluctuations of the impurity electron filling are described by the charge susceptibility $\chi_c \equiv \sum_m \chi_{c, m}$, which can also be expressed in terms of \tilde{A}_m and $\tilde{U}_{m, m'}$ using Eqs. (14) and (15):

$$\begin{aligned} \chi_{c, m} &\equiv -\sum_{m'} \frac{\partial \langle n_{dm} \rangle}{\partial \epsilon_{m'}} = \sum_{m'} \chi_{m, m'} \\ &= \tilde{A}_m(0) \left[1 - \sum_{m' (\neq m)} \tilde{U}_{m, m'} \tilde{A}_{m'}(0) \right]. \end{aligned} \quad (21)$$

The last line shows that the residual interaction $\tilde{U}_{m, m'}$ reduces the free-quasiparticle contributions given by the first term in the right-hand side.

C. Conductance and nonlinear susceptibilities

The conductance g_{tot} through a quantum dot can be expressed in the Landauer form [49–51],

$$g_{\text{tot}} = \sum_{m=1}^N g_m, \quad (22)$$

$$g_m = \frac{e^2}{h} \frac{4\Delta_L \Delta_R}{\Delta_L + \Delta_R} \int_{-\infty}^{\infty} d\omega \left(-\frac{\partial f(\omega)}{\partial \omega} \right) \pi A_m(\omega, T). \quad (23)$$

Here, $f(\omega) = 1/(e^{\omega/T} + 1)$ is the Fermi distribution function. It has recently been clarified that low-temperature behavior of conductance up to order T^2 can be determined completely by an extended Fermi-liquid theory [31–33]. This formulation is also applicable to the multilevel Anderson impurity model at arbitrary electron fillings, and the low-temperature expansion

can be expressed in the following form, for symmetric tunneling couplings $\Delta_L = \Delta_R$ [33,34],

$$g_m = \frac{e^2}{h} [\sin^2 \delta_m + c_{T,m} (\pi T)^2 + \dots]. \quad (24)$$

Here, the first term in the right-hand side corresponds to the ground-state value that is determined by the transmission probability $\sin^2 \delta_m$. The coefficient $c_{T,m}$ for the term of order T^2 consists of two parts [31–34]:

$$c_{T,m} = \frac{\pi^2}{3} [w_{T,m} + \theta_{T,m}], \quad (25)$$

$$w_{T,m} = -\cos 2\delta_m \left(\chi_{m,m}^2 + 2 \sum_{m'(\neq m)} \chi_{m,m'}^2 \right), \quad (26)$$

$$\theta_{T,m} = \frac{\sin 2\delta_m}{2\pi} \left(\chi_{m,m,m}^{[3]} + \sum_{m'(\neq m)} \chi_{m,m',m'}^{[3]} \right). \quad (27)$$

Here, $w_{T,m}$ represents the two-body contributions which are determined by the linear susceptibilities $\chi_{m,m'}$. The other part $\theta_{T,m}$ represents the three-body contributions, determined by the nonlinear susceptibilities [33,34],

$$\chi_{m_1,m_2,m_3}^{[3]} \equiv -\int_0^\beta d\tau_1 \int_0^\beta d\tau_2 \langle T_\tau \delta n_{dm_3}(\tau_3) \delta n_{dm_2}(\tau_2) \delta n_{dm_1} \rangle. \quad (28)$$

Here, T_τ is the imaginary time ordering operator. This correlation function corresponds also to the derivative of linear susceptibilities:

$$\chi_{m_1,m_2,m_3}^{[3]} = -\frac{\partial^3 \Omega}{\partial \epsilon_{m_1} \partial \epsilon_{m_2} \partial \epsilon_{m_3}} = \frac{\partial \chi_{m_2,m_3}}{\partial \epsilon_{m_1}}. \quad (29)$$

We note that $\chi_{m_1,m_2,m_3}^{[3]}$ vanishes in the case at which the system has both the particle-hole and time-reversal symmetries.

D. NRG approach to the spectral function and transport coefficients

The NRG has successfully been applied to multi-orbital quantum dots including CNT dots since a seminal work of Izumida *et al.* [10,11,37,40,52–55]. Using the NRG, we calculate the renormalized parameters such as the phase shifts of electrons δ , the wave-function renormalization factor Z , and the Wilson ratio R [56–58]. The present work uses the NRG to calculate not only the renormalized parameters, but also the linear conductance g and the spectral function $A_m(\omega, T)$ [21–23].

The key approximation of the NRG is the logarithmic discretization of the conduction band. A dimensionless parameter Λ (>1) controls the discretization. The noninteracting part of the discretized Hamiltonian $\mathcal{H}_d^0 + \mathcal{H}_T + \mathcal{H}_c$ is transformed into a one-dimensional tight-binding chain with exponentially decaying hopping matrix elements $t_n \sim D\Lambda^{-n/2}$. Then, the total Hamiltonian \mathcal{H} including the interactions can be diagonalized iteratively by adding the states on the tight-binding chain, starting from the impurity site. Owing to the exponential decay of t_n , high energy states can be discarded at each successive step without affecting low-lying energy states so much. Although this iteration itself is an artificial procedure, it can be interpreted as a process to probe

lower energy scale, step by step, starting from high-energy scale [21]. We briefly explain the process of the NRG iteration in Appendix B. Furthermore, we can deduce the quasiparticle parameters Z_m , $\tilde{\epsilon}_m$, and $\tilde{U}_{m,m'}$ from asymptotic behaviours of the low-lying eigenvalues near the NRG fixed point (see Appendix C) [22,23,48].

In the present work, we explore the CNT dots in a case where the fourfold degeneracy is not completely lifted by the magnetic field but still a double degeneracy remains for the reason which will be discussed in more detail in Sec. III B.

Our NRG code uses the $U(1) \otimes [SU(2) \otimes U(1)] \otimes U(1)$ symmetries to explore the $SU(4)$ to $SU(2)$ Kondo crossover. The $U(1) \otimes U(1) \otimes U(1) \otimes U(1)$ symmetries are used to examine how perturbations, i.e., the valley mixing and spin-orbit interaction, affect the crossover because the perturbations break the $SU(2)$ symmetry. The NRG calculations are carried out keeping typically the lowest 4100 states in the truncation procedure, choosing the discretization parameter to be $\Lambda = 6.0$. Furthermore, the spectral function and temperature-dependent conductance [59,60] are obtained using the complete Fock-space basis algorithm [24–26], together with the Oliveira *z averaging* [59,61]. For obtaining the spectral functions, we also calculate the higher-order correlation function in order to directly deduce the self-energy $\Sigma_m(\omega, T)$ [62]. These supplemental techniques for the dynamical correlations functions are also described in Appendix E.

III. FIELD-INDUCED $SU(4)$ TO $SU(2)$ CROSSOVER OF KONDO SINGLET STATE

A. Microscopic description for the CNT-dot levels

The Hamiltonian \mathcal{H} defined in Eqs. (1)–(4) are described using a representation in which the dot part \mathcal{H}_d^0 has already been diagonalized. However, to see a microscopic background, the other basis set using the spin (\uparrow, \downarrow) and valley (K, K') degrees of freedom is more suitable.

The valley degrees of freedom capture a magnetic moment along the CNT axis because of the cylindrical geometry of the CNT. This orbital moment couples to an external magnetic field parallel to the CNT axis [7,28,37,63,64]. The four levels of the CNT dot are also coupled each other through the spin-orbit interaction Δ_{SO} and the valley mixing $\Delta_{KK'}$. The dot part of the Hamiltonian can be expressed in the following form, using the dot-electron operator $\psi_{d:\ell s}^\dagger$ for orbital ℓ ($= K, K'$) and spin s ($= \uparrow, \downarrow$),

$$\mathcal{H}_d^0 \equiv \sum_{\ell, \ell'} \sum_{s, s'} \psi_{d:\ell s}^\dagger H_{d:\ell s, \ell' s'}^0 \psi_{d:\ell' s'} = \psi_d^\dagger \mathbf{H}_d^0 \psi_d. \quad (30)$$

The matrix $\mathbf{H}_d^0 \equiv \{H_{d:\ell s, \ell' s'}^0\}$ is given by [7,28,37]

$$\mathbf{H}_d^0 = \varepsilon_d \mathbf{1}_s \otimes \mathbf{1}_{\text{orb}} + \frac{\Delta_{KK'}}{2} \mathbf{1}_s \otimes \boldsymbol{\tau}^x + \frac{\Delta_{SO}}{2} \boldsymbol{\sigma}^z \otimes \boldsymbol{\tau}^z - \vec{\mathcal{M}} \cdot \vec{b}, \quad (31)$$

$$\vec{\mathcal{M}} \equiv -\frac{1}{2} g_s \vec{\sigma} \otimes \mathbf{1}_{\text{orb}} - g_{\text{orb}} \mathbf{1}_s \otimes \boldsymbol{\tau}^z \vec{e}_z. \quad (32)$$

Here, $\boldsymbol{\sigma}^j = \{\sigma_{ss'}^j\}$ and $\boldsymbol{\tau}^j = \{\tau_{\ell\ell'}^j\}$ for $j = x, y, z$ are the Pauli matrices for the spin and the valley pseudo-spin spaces, respectively. Correspondingly, $\mathbf{1}_s = \{\delta_{ss'}\}$ and $\mathbf{1}_{\text{orb}} = \{\delta_{\ell\ell'}\}$ are the corresponding unit matrices. In a finite magnetic field

$\vec{b} \equiv \mu_B \vec{B}$, where μ_B is the Bohr magneton, both the spin and orbital moments contribute to the magnetization $\vec{\mathcal{M}}$. The g factor for the spin is $g_s = 2.0$. The orbital moment couples to the magnetic field along the nanotube axis, and the orbital Zeeman splitting is given by $\pm g_{\text{orb}} |\vec{b}| \cos \Theta$. Here, g_{orb} is the orbital Landé factor and Θ is the angle of the magnetic field relative to the nanotube axis, which is chosen as the z axis with \vec{e}_z the unit vector. The one-particle Hamiltonian of the dot levels \mathbf{H}_d^0 can be diagonalized via the unitary transform with the matrix $\mathbf{U}_d = (\mathbf{u}_1, \mathbf{u}_2, \mathbf{u}_3, \mathbf{u}_4)$, constructed with the eigenvectors,

$$\mathbf{H}_d^0 \mathbf{u}_m = \epsilon_m \mathbf{u}_m, \quad \mathbf{u}_m^\dagger \cdot \mathbf{u}_{m'} = \delta_{mm'}. \quad (33)$$

The operator d_m that annihilates an electron in the eigenstate with energy ϵ_m can be expressed in a linear combination of $\psi_{d:\ell s}$'s via this transform with \mathbf{U}_d .

For $\Delta_{\text{SO}} = \Delta_{\text{KK}'} = 0$, the spin component of the magnetization becomes parallel to the field $\vec{e}_\Theta = \cos \Theta \vec{e}_z + \sin \Theta \vec{e}_x$ while the orbital component is in the direction along the nanotube axis ($\Theta \leq \pi/2$). Then, the eigenvalues of \mathbf{H}_d^0 can be written as $\epsilon_1 = \epsilon_d - (g_{\text{orb}} \cos \Theta + g_s/2)b$, $\epsilon_2 = \epsilon_d - (g_{\text{orb}} \cos \Theta - g_s/2)b$, $\epsilon_3 = \epsilon_d + (g_{\text{orb}} \cos \Theta - g_s/2)b$, and $\epsilon_4 = \epsilon_d + (g_{\text{orb}} \cos \Theta + g_s/2)b$. The eigenstates, for $m = 1, 2, 3$, and 4 , correspond to $|K' \downarrow_{\vec{b}}\rangle$, $|K' \uparrow_{\vec{b}}\rangle$, $|K \downarrow_{\vec{b}}\rangle$, and $|K \uparrow_{\vec{b}}\rangle$, respectively, with $\uparrow_{\vec{b}}$ and $\downarrow_{\vec{b}}$ the spin defined with respect to the direction along the field \vec{b} . Therefore the thermal average of $\vec{\mathcal{M}}$ can be written in the form

$$\langle \psi_d^\dagger \vec{\mathcal{M}} \psi_d \rangle = \mathcal{M}_{\text{orb}} \vec{e}_z + \mathcal{M}_s \vec{e}_\Theta, \quad (34)$$

$$\mathcal{M}_{\text{orb}} = g_{\text{orb}} [\langle n_{d1} \rangle - \langle n_{d4} \rangle + \langle n_{d2} \rangle - \langle n_{d3} \rangle], \quad (35)$$

$$\mathcal{M}_s = \frac{g_s}{2} [\langle n_{d1} \rangle - \langle n_{d4} \rangle - \langle n_{d2} \rangle + \langle n_{d3} \rangle]. \quad (36)$$

In more general cases, the matrix for $\vec{\mathcal{M}}$ with respect to one-particle eigenvector \mathbf{u}_m , can be expressed in the following forms using the Feynman theorem:

$$\vec{K}_m \equiv \mathbf{u}_m^\dagger \vec{\mathcal{M}} \mathbf{u}_m = -\mathbf{u}_m^\dagger \frac{\partial \mathbf{H}_d^0}{\partial \vec{b}} \mathbf{u}_m = -\frac{\partial \epsilon_m}{\partial \vec{b}}. \quad (37)$$

The thermal average of the magnetization $\vec{\mathcal{M}}$ can be written in terms of these matrix elements,

$$\vec{\mathcal{M}} \equiv \langle \psi_d^\dagger \vec{\mathcal{M}} \psi_d \rangle = \sum_m \vec{K}_m \langle n_{d,m} \rangle. \quad (38)$$

Therefore the magnetic susceptibility $\chi_{\mathcal{M}}^{\mu\nu} \equiv \partial \mathcal{M}^\mu / \partial b_\nu$, which is not isotropic for nano-tube dots, can be expressed in the following form:

$$\begin{aligned} \chi_{\mathcal{M}}^{\mu\nu} &= \sum_m \frac{\partial K_m^\mu}{\partial b_\nu} \langle n_{d,m} \rangle + \sum_{m,m'} K_m^\mu \frac{\partial \epsilon_{m'}}{\partial b_\nu} \frac{\partial \langle n_{d,m} \rangle}{\partial \epsilon_{m'}} \\ &= \sum_m \frac{\partial K_m^\mu}{\partial b_\nu} \langle n_{d,m} \rangle + \sum_{m,m'} K_m^\mu K_{m'}^\nu \chi_{m,m'}, \\ &= \sum_m \frac{\partial K_m^\mu}{\partial b_\nu} \langle n_{d,m} \rangle + \sum_m K_m^\mu K_m^\nu \tilde{A}_m \\ &\quad - \sum_{m \neq m'} K_m^\mu K_{m'}^\nu \tilde{A}_m \tilde{A}_{m'} \tilde{U}_{mm'}. \end{aligned} \quad (39)$$

Here, the last term in the right-hand side represents the contributions of the residual interaction, or the vertex corrections. Since the Wilson ratio $R_{m,m'}$ given in Eq. (18) depends on the residual interaction, $R_{m,m'}$ relates to the magnetic susceptibilities.

B. CNT level structure and field-induced crossover

In recent experiments reported in Refs. [19,35], nonlinear current and current noise were measured for a CNT dot with the orbital Landé factor $g_{\text{orb}} \approx 4$ at finite magnetic fields with an angle $\Theta \approx 75^\circ$. These values of g_{orb} and Θ imply that the magnitude of the orbital Zeeman splitting becomes almost the same as the spin Zeeman splitting in this particular situation,

$$g_{\text{orb}} \cos \Theta \approx \frac{1}{2} g_{\text{orb}} = 1. \quad (40)$$

This situation can take place for CNT dots as the orbital Landé factor g_{orb} depends significantly on the diameter of nanotube and takes a value around $g_{\text{orb}} \sim 10$ [7]. In the case where this matching of the orbital and spin Zeeman splittings is satisfied, the energy level of the dot has a double degeneracy which remains unlifted in magnetic fields:

$$\epsilon_1 = \epsilon_d - 2b, \quad \epsilon_2 \equiv \epsilon_3 = \epsilon_d, \quad \epsilon_4 = \epsilon_d + 2b. \quad (41)$$

In this case, the occupation numbers of the degeneracy become the same $\langle n_{d2} \rangle = \langle n_{d3} \rangle$. Thus both the orbital and spin magnetizations are determined by the occupation numbers of the other two levels $m = 1$ and $m = 4$: $\mathcal{M}_{\text{orb}} = g_{\text{orb}} \mathcal{M}_{14}$ and $\mathcal{M}_s = \frac{g_s}{2} \mathcal{M}_{14}$, with

$$\mathcal{M}_{14} \equiv \langle n_{d1} \rangle - \langle n_{d4} \rangle. \quad (42)$$

We note that Δ_{SO} and $\Delta_{\text{KK}'}$ are less important for the examined CNT dot [19,35,36]. In this situation, the system has an SU(2) rotational symmetry defined with respect to the degenerate states in the middle, and the U(1) symmetry that conserves the sum of the occupation numbers $n_2 + n_3$, in addition to the other two U(1) symmetries corresponding to n_1 and n_4 for the levels $m = 1$ and $m = 4$, respectively. Therefore the SU(4) symmetry that the total Hamiltonian has at zero field breaks down to the $U(1)_{m=1} \otimes [SU(2) \otimes U(1)]_{m=2,3} \otimes U(1)_{m=4}$ symmetry at finite magnetic fields. This SU(2) symmetric part plays a central role in the field-induced SU(4) to SU(2) Kondo crossover, occurring at half-filling point $N_d = 2$. At this point, due to the matching condition given in Eq. (41), the Hamiltonian \mathcal{H} is invariant under an extended electron-hole transformation described by Eq. (A5).

C. Comparison of NRG and experiments results: gate-voltage dependence at finite B or T

We have shown in the previous work [35,36] that the level scheme, given in Eq. (41), nicely explains the field-induced SU(4) to SU(2) Kondo crossover observed at half-filling $N_d = 2$ where two electrons occupy the local levels of the CNT dot. The Coulomb interaction for this CNT dot is estimated to be $U \approx 6$ meV, and the hybridization energy is $\Delta \equiv \Delta_L + \Delta_R \approx 0.9$ meV. Its asymmetric factor is $4\Delta_L \Delta_R / (\Delta_L + \Delta_R)^2 = 0.92$. The energy scales the interaction as $U / (\pi \Delta) = 2.0$. The

SU(4) Kondo temperature for the scaled U is $T_K^{\text{SU}(4)}/\Delta = 0.41$ which corresponds to $T_K = 4.3$ K in a real scale. These values of U and Δ are much larger than the value of the valley mixing $\Delta_{KK'}$ and than that of the spin-orbit interaction Δ_{SO} . The experimental values of $\Delta_{KK'}$ and Δ_{SO} are $\Delta_{KK'} \simeq \Delta_{\text{SO}} \approx 0.2$ meV. We note that these values depend on the detailed structures of carbon nanotube samples. Furthermore, it has also estimated in the experiment that the orbital Zeemann coupling as $g_{\text{orb}} \cos \theta \simeq 0.7$ [35], which is not so far from the matching condition $g_{\text{orb}} \cos \theta = 1$, described in Eq. (40).

We first of all discuss the magnetoconductance for the case $g_{\text{orb}} \cos \theta = 1$ and $\Delta_{KK'} = \Delta_{\text{SO}} = 0$, at which an ideal SU(4) to SU(2) Kondo crossover occurs. Figure 1(a) compares the NRG results of the conductance at $T = 0$ with the experimental results obtained at $T = 16$ mK. The values of U and Δ for the NRG calculations are the experimental values. The comparisons which have been done also in Ref. [35] show that the NRG results nicely agree with the experimental results. We can clearly see in this figure that the Kondo ridge emerges near half-filling $V_g \simeq 26$ V in the absence and presence of magnetic fields. Its height reduces from the SU(4) value $3.68 e^2/h$ to the SU(2) value $1.84 e^2/h$ as magnetic field increases. This reduction of the height implies that the observed SU(2) behavior is caused by the doubly degenerate states, which are labeled as $m = 2$ and 3 in Eq. (41), are shifted towards the Fermi level in the half-filled case where $\epsilon_d = -3U/2$. Furthermore, the additional subpeaks, which emerge outside the Kondo ridge for large magnetic fields $B \gtrsim 4$ T, can also be regarded as the resonances corresponding to the other two nondegenerate levels, labeled as $m = 1$ and 4. Note that the Kondo ridges corresponding to the 1/4 and 3/4 fillings are not so pronounced at $B = 0$ because the Coulomb interaction for this CNT dot $U/(\pi\Delta) = 2.0$ is not very large.

We also examine the case where the matching condition described in Eq. (40) cannot be satisfied, taking the parameters such that $\Delta_{KK'} = \Delta_{\text{SO}} = 0.2$ meV and $g_{\text{orb}} \cos \theta = 0.7$.¹ At zero field $b = 0$, the level structure is given by

$$\epsilon_1 = \epsilon_2 = \epsilon_d - \frac{1}{2} \sqrt{\Delta_{KK'}^2 + \Delta_{\text{SO}}^2}, \quad (43)$$

$$\epsilon_3 = \epsilon_4 = \epsilon_d + \frac{1}{2} \sqrt{\Delta_{KK'}^2 + \Delta_{\text{SO}}^2}. \quad (44)$$

The value of the gap due to the spin-orbit interaction and valley mixing is $\sqrt{\Delta_{KK'}^2 + \Delta_{\text{SO}}^2} \simeq 0.28$ meV, which is smaller than the resonance width. Figure 1(b) shows the NRG results, obtained taking the other parameters the same as those for Fig. 1(a), i.e., $U/(\pi\Delta) = 2.0$, $\Delta = 0.9$ meV. The broad peak emerges also in Fig. 1(b) although its peak value $3.14 e^2/h$ is smaller than that the value $3.68 e^2/h$, which is for the case of $\Delta_{KK'} = \Delta_{\text{SO}} = 0$ and $g_{\text{orb}} \cos \theta = 1$. The flat structure is still preserved in small magnetic fields up to $B \approx 5$ T. This preservation shows that the SU(4) to SU(2) Kondo crossover is robust against the perturbations. The larger magnetic fields $B \gtrsim 5$ T split the peak into two peaks. Furthermore, other two sub peaks grow with increasing B , and thus the four distinct peaks emerge. Figure 1(b) shows that the magnetoconductance for $B = 10$ T has the four peaks.

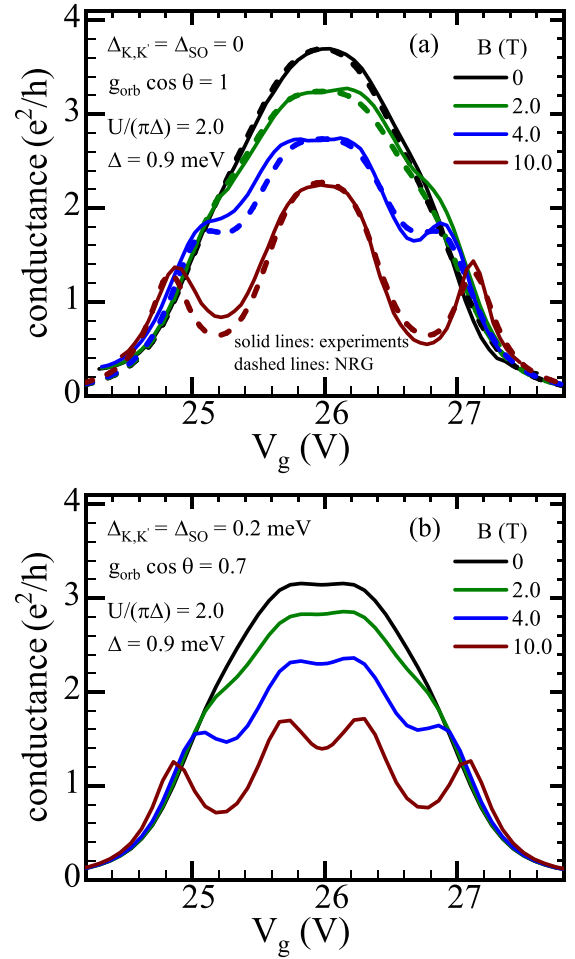


FIG. 1. (a) and (b) plot the zero temperature conductance as functions of experimental gate voltages V_g for four values of magnetic fields: $B = 0, 2, 4,$ and 10 T. In the CNT dot where the experiments observed the crossover, the experimental V_g relates to theoretical the theoretical ϵ_d via a linear relation: $V_g = (0.8\epsilon_d/U + 27.18)$ in units of volt. The asymmetric factor in Eq. (23) and the Coulomb interaction are respectively $4\Delta_L\Delta_R/\Delta^2 = 0.92$ and $U/(\pi\Delta) = 2.0$ for each two figure. Here, $\Delta \equiv \Delta_L + \Delta_R = 0.9$ meV. In (a), the dashed lines and solid lines respectively represent NRG and experimental results. The NRG results plotted in (a) are for parameters: $\Delta_{\text{SO}} = \Delta_{KK'} = 0$, $g_{\text{orb}} \cos \theta = 1$. The experimental results have been obtained at $T = 16$ mK [19,35], which is much lower than $T_K^{\text{SU}(4)} = 4.3$ K, the Kondo temperature for the half-filled case (at $V_g \simeq 26$ mV). (b) plots only NRG results by solid lines. The parameters for the results are $\Delta_{\text{SO}} = \Delta_{KK'} = 0.2$ meV and $g_{\text{orb}} \cos \theta = 0.7$.

Our NRG results for the CNT dots, reported so far, were restricted to ground-state properties. The present work sheds light also on the finite-temperature and dynamic properties of the Kondo crossover. Figure 2 compares the experimental results [35] of the zero-field conductance measured at $T = 16$ mK, 2 K, and 4.5 K with the corresponding NRG results, calculated for slightly lower temperatures $T = 0$ K, 1.7 K, and 3.8 K to demonstrate how these comparisons work at the best. We see a reasonable agreement between the theoretical results and experimental results. The height of the Kondo ridge emerging near half-filling $V_g \simeq 26$ V decreases as temperature

¹See Supplemental Material of Ref. [35].

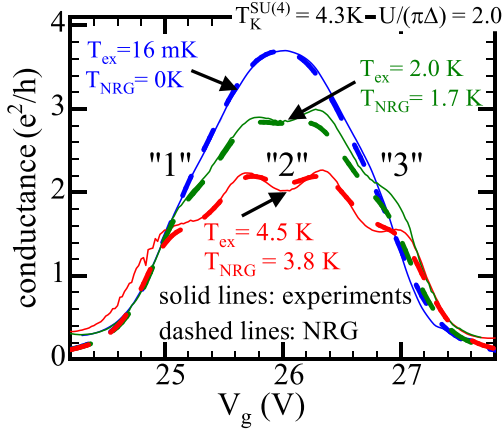


FIG. 2. Zero-field, $B = 0$, conductance at finite temperatures: experimental (solid line) and NRG (dashed line) results are plotted vs V_g . The experimental data has been obtained at $T = 16$ mK, 2 K, and 4.5 K [19]. For NRG calculations, slightly lower temperatures $T = 0, 1.7$, and 3.8 K are chosen. The other parameters are the same as those used for Fig. 1. The numbers “3,” “2,” and “1” shown in these two figures represent the electron filling N_d at corresponding V_g .

increases. At temperatures of order $T \sim T_K^{\text{SU}(4)} = 4.3$ K, four peaks corresponding to the Coulomb oscillation emerge. This agreement also indicates that the theory of the SU(4) Kondo effect can explain the experimental results of the conductance.

D. Scaling behavior of SU(4) conductance at quarter and half-filling

In this section, we examine scaling behavior of the SU(4) conductance as functions of temperature especially at quarter-filling $N_d = 1$ and half-filling $N_d = 2$. In Fig. 2, the valley is quarter and half-filled at gate voltages, $V_g \simeq 25$ V and $V_g \simeq 26$ V, respectively. The first value of V_g corresponds to the theoretical value $\epsilon_d/U = -1/2$, and the second one corresponds to $\epsilon_d/U = -3/2$.

Since the T^2 coefficient $c_{T,m}$ of conductance given in Eq. (25) depends on linear and nonlinear susceptibilities, we discuss properties of these susceptibilities to examine the scaling. In the SU(N) symmetric case at which the N impurity levels are degenerate $\epsilon_m \equiv \epsilon_d$, the linear susceptibilities have only two independent elements: a diagonal element $\chi_{m,m}$ and the off-diagonal element $\chi_{m,m'}$ for $m \neq m'$. The diagonal element determines a characteristic energy scale T^* ,

$$T^* \equiv \frac{1}{4\chi_{m,m}}. \quad (45)$$

In the particle-hole symmetric case $\epsilon_d/U \rightarrow -(N-1)/2$, it corresponds to the renormalized width of the Kondo resonance as $T^* \rightarrow (\pi/4)\Delta$. At any arbitrary electron fillings, T^* scales the impurity specific heat defined in Eq. (20) as $C_{\text{dot}} = \frac{N\pi^2}{12}(T/T^*)$.

In the SU(N) symmetric case, the Wilson ratio R defined in Eq. (18) also takes a simplified form $R - 1 = -\chi_{m,m'}/\chi_{m,m}$, where the flavour index has been dropped in the left-hand side. The Wilson ratio takes the maximum value in the strong

coupling limit $U \rightarrow \infty$ at integer filling points:

$$R_{\text{SU}(N)}^{\text{max}} - 1 \xrightarrow{U \rightarrow \infty, N_d \rightarrow \text{integer}} \frac{1}{N-1}. \quad (46)$$

This is because the charge fluctuations are suppressed in this limit, and the charge susceptibility defined in Eq. (21) vanishes: $\chi_{c,m} = \chi_{m,m} + (N-1)\chi_{m,m'} \rightarrow 0$.

The nonlinear susceptibilities have three independent elements in the SU(N) symmetric case for $N > 2$: $\chi_{m,m,m}^{[3]}$, $\chi_{m,m',m'}^{[3]}$, and $\chi_{m,m',m''}^{[3]}$, where $m \neq m'$, $m' \neq m''$, and $m \neq m''$. We note that the derivative of the diagonal linear susceptibility $\chi_{m,m}$ with respect to ϵ_d can be related to the first two elements, as

$$\frac{\partial \chi_{m,m}}{\partial \epsilon_d} = \chi_{m,m,m}^{[3]} + (N-1)\chi_{m,m',m'}^{[3]}. \quad (47)$$

We next revisit the temperature dependence of conductance for the SU(N) Anderson model, which has been previously studied in detail by Anders *et al.* [12], taking in a recent Fermi-liquid viewpoint [31–34]. The low-energy expansion, given in Eqs. (24) and (25), takes the following form in the SU(N) symmetric case,

$$g_{\text{tot}} = \frac{N e^2}{h} \left[\sin^2 \delta - C_T \left(\frac{\pi T}{T^*} \right)^2 + \dots \right], \quad (48)$$

$$C_T \equiv \frac{\pi^2}{48} (W_T + \Theta_T). \quad (49)$$

The two-body contributions W_T and three-body contributions Θ_T , defined respectively in Eqs. (26) and (27), can be rewritten in the following form using also Eq. (47),

$$W_T \equiv -[1 + 2(N-1)(R-1)^2] \cos 2\delta, \quad (50)$$

$$\Theta_T = \frac{\sin 2\delta}{2\pi} \frac{1}{\chi_{m,m}^2} \frac{\partial \chi_{m,m}}{\partial \epsilon_d}. \quad (51)$$

Figures 3(a) and 3(b) show the temperature dependence of g_{tot} at half-filling and quarter-filling, respectively. We choose four values of the interaction, $U/(\pi\Delta) = 2.0, 3.0, 4.0$, and 5.0. The first value is the experimental value for the valley where the SU(4) Kondo effect occurs. In other valleys, the experimental values of $U/(\pi\Delta)$ can be larger than 2.0, and we also consider the larger interaction cases. The temperatures are scaled by the Kondo energy scales T^* defined in Eq. (45) for each N_d and U . In each of the two figures, we find that the scaled conductance curves collapse into a single curve over a wide range of temperatures $T \lesssim T^*$ for $U/(\pi\Delta) \gtrsim 3.0$, and thus the conductance shows the universality for each filling.

To clarify the filling dependence of the universality, we replot the curves of quarter and half filling in Fig. 3(c). For the two curves, we choose the largest U among the four, $U/(\pi\Delta) = 5.0$. We find that whereas these two curves almost overlap each other around $T \simeq T^*$, the conductance of quarter-filling is slightly larger than that of half-filling at low-temperatures $T < T^*$, especially around $T \simeq 0.1T^*$. The inset of Fig. 3(c) clearly shows the different behavior depending on the filling.

This filling dependence of the scaling can be explained by the Fermi-liquid theory [31–34]. We have recently clarified using also the NRG that the derivative of the diagonal

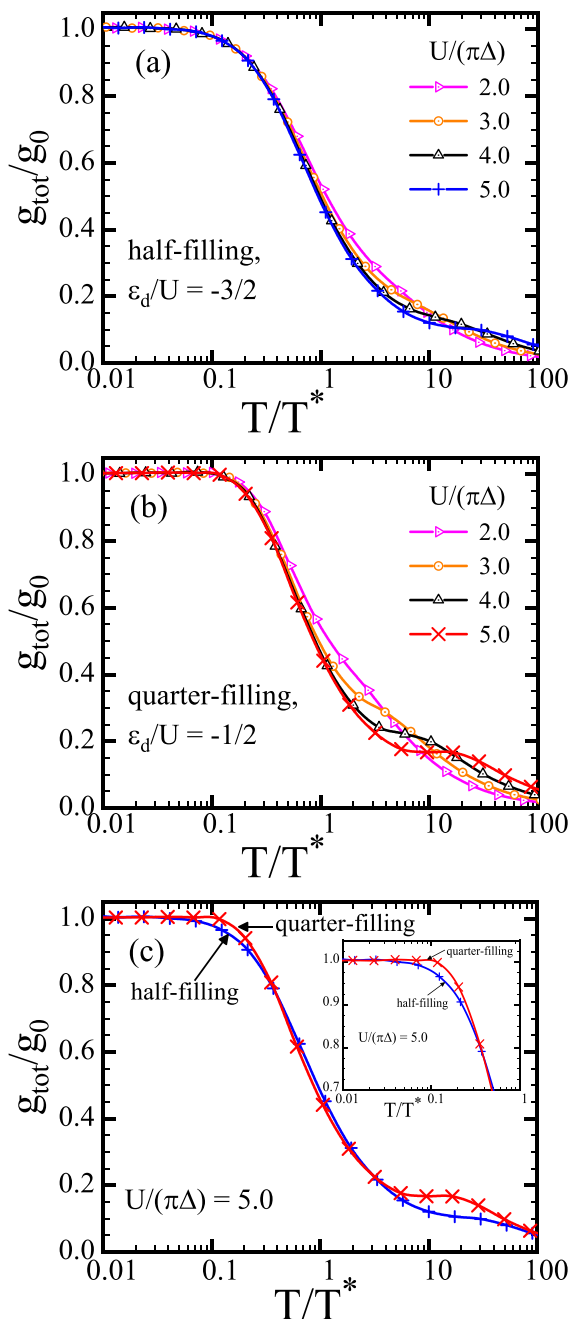


FIG. 3. SU(4) conductance curves are plotted as functions of temperature T . (a) and (b) show the results at half-filling and quarter-filling, respectively. In these figures, the conductance curves are plotted for four values of the interaction, $U/(\pi\Delta) = 2.0, 3.0, 4.0,$ and 5.0 . (c) shows the curves of half-filling and quarter-filling for the largest value $U/(\pi\Delta) = 5.0$. The inset of (c) is an enlarged view for $0.01 \leq T/T^* \leq 1$. This inset clearly shows that the T^2 coefficient C_T given in Eq. (49) vanishes at quarter-filling whereas that at half-filling does not. In (a)–(c), the x axis is scaled by the Kondo temperature $T^* \equiv 1/(4\chi_{m,m})$. The values of T^*/Δ at half-filling are 0.41, 0.29, 0.20, and 0.13 for $U/(\pi\Delta) = 2.0, 3.0, 4.0,$ and 5.0 , respectively. Similarly, the values at quarter-filling are 0.82, 0.57, 0.37, and 0.23. The y -axis is normalized by the zero temperature values of conductance, $g_0 = (4e^2/h) \sin^2 \delta$. At half-filling, $\sin^2 \delta \equiv 1$ for any value of U , and at quarter-filling, $\sin^2 \delta = 0.56, 0.55, 0.54,$ and 0.54 .

susceptibility $|\partial \chi_{m,m}/\partial \epsilon_d|$ becomes much smaller than $\chi_{m,m}^2$ in a wide region of electron fillings $1 \lesssim N_d \lesssim 3$ for large interactions $U \gg \Delta$ [34]. From this result, it follows that the three-body contributions Θ_T given by Eq. (51) almost vanish in the same region, and the T^2 conductance in this case is determined by the two-body contributions, as

$$C_T \simeq -(\pi^2/48)[1 + 6(R-1)^2] \cos(\pi N_d/2). \quad (52)$$

Thus C_T becomes 0 at quarter filling $N_d = 1$, whereas it is finite $C_T = (\pi^2/48)[1 + 6(R-1)^2]$ at half-filling $N_d = 2$. Therefore the conductance at $N_d = 1$ persists the zero temperature value at $0 \leq T/T^* \simeq 0.1$ as shown in the inset of Fig. 3(c). At $N_d = 2$, the coefficient approaches $C_T^\infty = 5\pi^2/144 \simeq 0.3427$ at $U \rightarrow \infty$. This is because the Wilson ratio for $N = 4$ saturates to the strong coupling limit value $R_{\text{SU}(4)}^{\text{max}} - 1 \rightarrow 1/3$. Already at $U/(\pi\Delta) = 3.0$, the coefficient is given by $C_T \simeq 0.34$, which is very close to the strong-coupling value C_T^∞ .

IV. EVOLUTION OF QUASIPARTICLES ALONG THE FIELD-INDUCED CROSSOVER

The Fermi-liquid parameters for renormalized quasiparticles describe low energy properties of quantum dots. The phase shift δ_m , which is the primary parameter, corresponds to zero temperature transmission probability. The renormalization factor Z_m and the Wilson ratio $R_{m,m'}$ are also important parameters to examine the higher-order properties of the Fermi-liquid states. We describe how these and related parameters evolve along a field induced crossover from the SU(4) to SU(2) Kondo singlet state. The crossover occurs for the dot levels defined in Eq. (41). Specifically, we consider the half-filled case corresponding to the point $V_g \simeq 26$ V in the middle of the Kondo ridge seen in Fig. 1. The center of the dot levels is chosen to be $\epsilon_d = -(3/2)U$, and thus the average number of electrons in the dot levels conserves in a way such that $\langle n_{d2} \rangle = \langle n_{d3} \rangle = 1/2$ and $\langle n_{d1} \rangle + \langle n_{d4} \rangle = 1$ at finite magnetic fields.

We examine two different values for the Coulomb interaction in the following: (i) $U/(\pi\Delta) = 2.0$ and (ii) $U/(\pi\Delta) = 4.0$. The first one, (i), simulates the situation of the CNT dot, in which the field-induced crossover has been observed and the parameters have been estimated as $U \approx 6$ meV and $\Delta \approx 0.9$ meV [19,35]. We can see more clearly the renormalization effects due to strong correlations in the second case (ii).

A. Fermi-liquid parameters for the real CNT dot

First of all, we consider the case $U/(\pi\Delta) = 2.0$ that is estimated by the recent experiments. The NRG results for this case are shown in Fig. 4. Figure 4(a) shows the transmission probability $\mathcal{T}_m(0) = \sin^2 \delta_m$ and magnetization $\mathcal{M}_{14} \equiv \langle n_{d1} \rangle - \langle n_{d4} \rangle$, as a function of magnetic field b at half-filling. The degenerate levels, $m = 2$ and 3 , keep their positions just on the Fermi level for finite magnetic fields, and show the unitary limit transport $\sin^2 \delta_m = 1$ as $\delta_2 = \delta_3 = \pi/2$. The magnetic field partly lifts the degeneracy and the other two states, $m = 1$ and 4 . For these orbitals, $\sin^2 \delta_m$ decreases as magnetic field increases. The magnetization \mathcal{M}_{14} , which in the present case is determined by the occupation number or

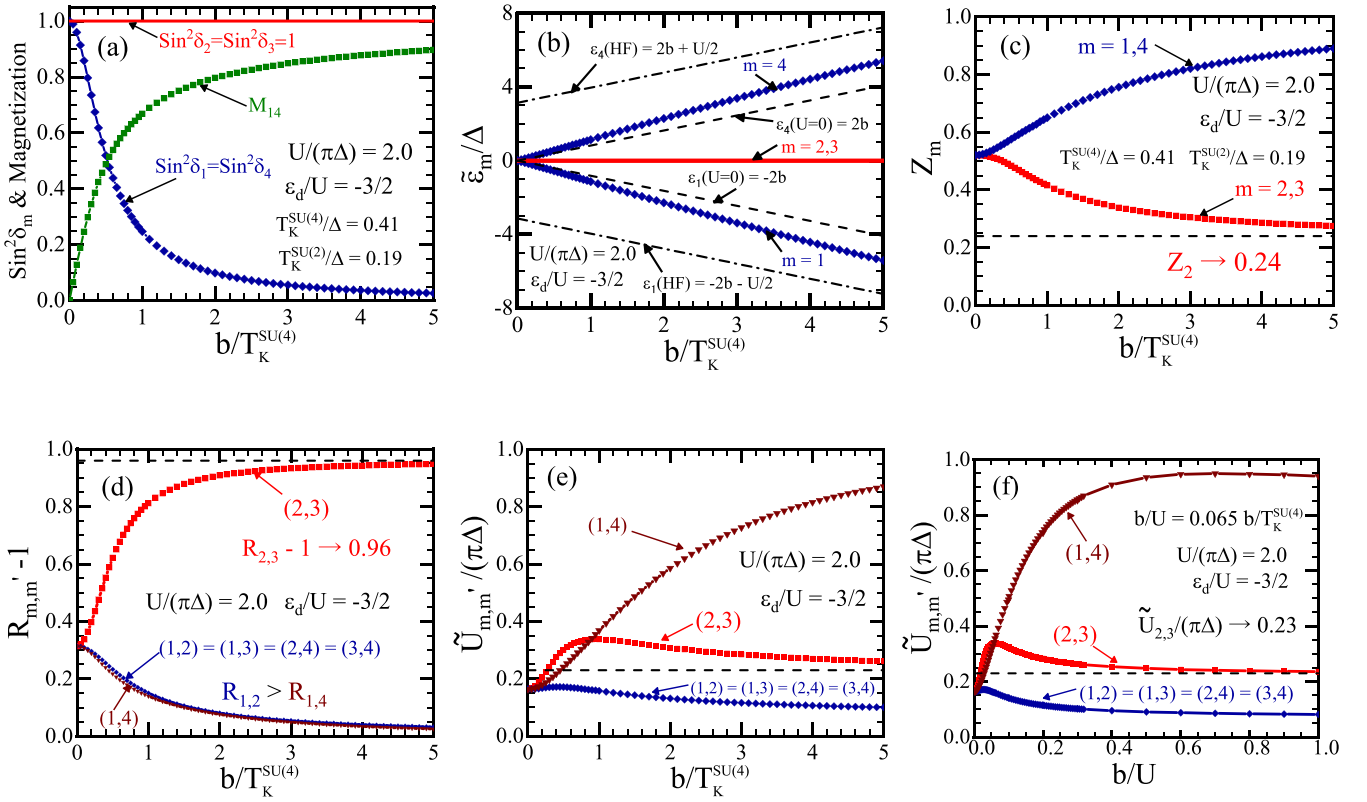


FIG. 4. (a) $\sin^2 \delta_m$ and magnetization $\mathcal{M}_{14} = \langle n_{d1} \rangle - \langle n_{d4} \rangle$, (b) renormalized level position $\tilde{\epsilon}_m$, (c) renormalization factor Z_m , (d) Wilson ratio $R_{m,m} - 1$, and (e) residual interaction $\tilde{U}_{m,m}$ are plotted as functions of magnetic field b at half-filling $\epsilon_d/U = -3/2$ for $U/(\pi\Delta) = 2.0$. The x axis in (a)–(e) is scaled by the SU(4) Kondo temperature $T_K^{\text{SU}(4)} = 0.41\Delta = (0.065U)$ determined at $b = 0$. In (f) the axis is scaled by U for examining the behavior of $\tilde{U}_{m,m}$ at larger magnetic fields $b > T_K^{\text{SU}(4)}$. The dot levels ϵ_m are chosen in a such way that is described in Eq. (41). In (b), the dashed lines indicate the bare Zeemann splitting, and the dash-dotted lines indicate the mean-field splitting $\epsilon_1^{\text{HF}} = -(2b + U/2)$ and $\epsilon_4^{\text{HF}} = (2b + U/2)$. In a similar way, the dashed lines in (c)–(f) indicate the SU(2) symmetric values of $Z_2 \rightarrow 0.23$, $R_{2,3} \rightarrow 1.96$, and $\tilde{U}_{2,3}/\pi\Delta \rightarrow 0.026$, respectively.

these two levels, increases as the magnetic field increases. It saturates to $\mathcal{M}_{14} \rightarrow 1$ in the limit of $b \rightarrow \infty$, and the charge fluctuations are suppressed as $\langle n_{d,1} \rangle \rightarrow 1$ and $\langle n_{d,4} \rangle \rightarrow 0$.

Figure 4(b) shows the renormalized resonance level position $\tilde{\epsilon}_m$ as a function of magnetic field b . The twofold degenerate states at the center, $\tilde{\epsilon}_2 = \tilde{\epsilon}_3 = 0$, remain just on the Fermi level at arbitrary magnetic fields. The other two levels, $\tilde{\epsilon}_1$ and $\tilde{\epsilon}_4$ move away from the Fermi level as b increases. Slopes of them are steeper than those for the noninteracting electrons $2b$ (dashed line). In the large field limit $b \rightarrow \infty$, the renormalized level positions approach the one described in the mean-field theory, i.e., $\epsilon_1^{\text{HF}} = -(2b + U/2)$ and $\epsilon_4^{\text{HF}} = (2b + U/2)$. These asymptotic form can be obtained as follows, substituting the mean values $\langle n_{d1} \rangle = 1$, $\langle n_{d4} \rangle = 0$ and $\langle n_{d2} \rangle = \langle n_{d3} \rangle = 1/2$ into the dot-part of the Hamiltonian with $\epsilon_d = -(3/2)U$;

$$\begin{aligned} \mathcal{H}_d^0 + \mathcal{H}_U &= 2b(n_{d4} - n_{d1}) - \frac{3U}{2}(n_{d2} + n_{d3} + n_{d1} + n_{d4}) \\ &+ U[n_{d2}n_{d3} + n_{d1}n_{d4} + (n_{d2} + n_{d3})(n_{d1} + n_{d4})] \\ &\xrightarrow{b \rightarrow \infty} U\left[n_{d2}n_{d3} - \frac{1}{2}(n_{d2} + n_{d3})\right] \\ &+ \left(2b + \frac{U}{2}\right)(n_{d4} - n_{d1}) + \text{const.} \end{aligned} \quad (53)$$

Here, the Coulomb interaction between the orbitals $m = 2$ and 3 is kept uncoupled. This asymptotic Hamiltonian also shows that the symmetric SU(2) Anderson model describes the Fermi-liquid properties of these two orbitals.

The magnetic field dependence of the wavefunction renormalization factors Z_m plotted in Fig. 4(c) more clearly shows the crossover. At finite magnetic fields, only two of the four Z_m 's become independent: $Z_2 = Z_3$ and $Z_1 = Z_4$ because of the particle-hole symmetry given in Eq. (A5). The first one is for the degenerate levels remaining on the Fermi level, and the second one is for the levels moving away from the Fermi level. At zero field, where the system has the SU(4) symmetry, these two factors for the different orbitals become identical each other: $Z_2 = Z_1 = Z_{\text{SU}(4)} = 0.52$ for $U/(\pi\Delta) = 2.0$. Substituting this SU(4) value into Eq. (45) gives the SU(4) Kondo energy scale $T_K^{\text{SU}(4)}/\Delta = 0.41$. Many-body effects significantly renormalize Z_2 from the SU(4) value as magnetic field increases. In the limit of $b \rightarrow \infty$, it approaches the SU(2) symmetric value $Z_{\text{SU}(2)} = 0.23$, which determines the SU(2) Kondo energy scale $T_K^{\text{SU}(2)}/\Delta = 0.19$. The many-body effects become less important for Z_1 with increasing field, and Z_1 approaches the noninteracting value $Z_1 \rightarrow 1$ for the large magnetic field.

In order to clarify the many-body effects between electrons occupying the different orbitals, we also examine the orbital dependent Wilson ratio $R_{m,m'}$ and corresponding residual interaction $\tilde{U}_{m,m'}$. Figures 4(d) and 4(e) respectively show $R_{m,m'} - 1$ and $\tilde{U}_{m,m'}$ as functions of $b/T_K^{\text{SU}(4)}$. Magnetic field dependences of $\tilde{U}_{m,m'}$ are plotted also in Fig. 4(f), where the magnetic field is scaled by U to examine behaviours of $\tilde{U}_{m,m'}$ at larger fields $b \gg T_K^{\text{SU}(4)}$. Owing to the particle-hole symmetry, only three of the six $\tilde{U}_{m,m'}$ are independent: $\tilde{U}_{2,3}$, $\tilde{U}_{1,4}$, and $\tilde{U}_{1,2} = \tilde{U}_{1,3} = \tilde{U}_{2,4} = \tilde{U}_{3,4}$. Correspondingly, three independent parameters of the Wilson ratios, $R_{2,3}$, $R_{1,4}$, and $R_{1,2}$, can be deduced from Eq. (18):

$$R_{2,3} - 1 = \frac{1}{Z_2} \frac{\tilde{U}_{2,3}}{\pi \Delta}, \quad (54)$$

$$R_{1,4} - 1 = \frac{\sin^2 \delta_1}{Z_1} \frac{\tilde{U}_{1,4}}{\pi \Delta}, \quad (55)$$

$$R_{1,2} - 1 = \sqrt{\frac{\sin^2 \delta_1}{Z_1} \frac{1}{Z_2} \frac{\tilde{U}_{1,2}}{\pi \Delta}}. \quad (56)$$

Among the three independent parameters of $R_{m,m'}$ and $\tilde{U}_{m,m'}$, $R_{2,3} - 1$ and $\tilde{U}_{2,3}$ are for the doubly degenerate orbitals on the Fermi level. At zero field, $R_{2,3}$ and $\tilde{U}_{2,3}$ take the SU(4) values $R_{2,3} - 1 = 0.31$ and $\tilde{U}_{2,3}/(\pi \Delta) = 0.16$ for $U/(\pi \Delta) = 2.0$, and $R_{2,3} - 1$ already approaches very closely to the value for the infinite Coulomb interaction: $R_{\text{SU}(4)}^{\text{max}} - 1 \equiv 1/3$. These parameters continuously evolve from the SU(4) values to the SU(2) symmetric values: $R_{\text{SU}(2)} - 1 = 0.96$ and $\tilde{U}_{2,3}/(\pi \Delta) = 0.23$.

We also discuss the field dependence of the other parameters, $R_{1,2}$, $R_{1,4}$, $\tilde{U}_{1,2}$, and $\tilde{U}_{1,4}$. $\tilde{U}_{1,2}$ decreases from the SU(4) value with increasing magnetic field, and the corresponding Wilson ratio $R_{1,2} - 1$ decreases to the noninteracting value 0. In contrast to $\tilde{U}_{1,2}$, $\tilde{U}_{1,4}$ increases from the zero field value and becomes larger than $\tilde{U}_{2,3}$ and $\tilde{U}_{1,2}$ for $b > T_K^{\text{SU}(4)}$. It further increases at the larger magnetic field regions $b \gg T_K^{\text{SU}(4)}$ as shown in Fig. 4(f). This field dependence of $\tilde{U}_{1,4}$ is similar to that of \tilde{U} for a single orbital Anderson model [65,66], although $\tilde{U}_{1,4}$ does not approach to the bare value U . We briefly discuss the field dependence of \tilde{U} and of the other Fermi liquid parameters for the single orbital Anderson model in Appendix D. This enhancement of $\tilde{U}_{1,4}$ does not result in the enhancement of $R_{1,4}$. In fact, $R_{1,4} - 1$ as well as $R_{1,2} - 1$ decreases to 0 since the factor $\sin^2 \delta_1$ goes to 0. We note that $R_{1,2}$ is slightly larger than $R_{1,4}$ at arbitrary b in this case of $U/(\pi \Delta) = 2.0$.

B. Fermi-liquid parameters for larger U

We next consider a strong coupling case, taking the Coulomb repulsion to be $U/(\pi \Delta) = 4.0$, which is twice as large as the one studied in the above. For this case, effects of the interactions on the field-induced SU(4) to SU(2) Kondo crossover emerges in a pronounced way. Such a situation is also realistic because the experimental values of U and Δ depend on individual quantum dots and on the valleys to be measured.

Figure 5(a) plots ground-state values of $\mathcal{T}_m(0) = \sin^2 \delta_m$ and of \mathcal{M}_{14} as functions of magnetic fields $b/T_K^{\text{SU}(4)}$ for

both $U/(\pi \Delta) = 4.0$ and $U/(\pi \Delta) = 2.0$. The results for $U/(\pi \Delta) = 4.0$ and $U/(\pi \Delta) = 2.0$ are plotted with solid lines and dashed lines, respectively. The energy scale depends on the coupling constant as $T_K^{\text{SU}(4)}/\Delta = 0.2$ for $U/(\pi \Delta) = 4.0$ and $T_K^{\text{SU}(4)}/\Delta = 0.41$ for $U/(\pi \Delta) = 2.0$. We see that $\sin^2 \delta_m$ and M_d of $U/(\pi \Delta) = 4.0$ show almost same b dependences as those of $U/(\pi \Delta) = 2.0$, and thus they show the universality. The universal behavior is determined by the b dependence of a single parameter $\delta_1 (= \pi - \delta_4)$. Renormalized levels $\tilde{\varepsilon}_m$ for $U/(\pi \Delta) = 4.0$ plotted in Fig. 5(b) show the different b dependence from those for $U/(\pi \Delta) = 2.0$. Specifically, $\tilde{\varepsilon}_1$ and $\tilde{\varepsilon}_4$ stay closer to the Fermi level than those for $U/(\pi \Delta) = 2.0$. However, this different b dependence does not affect the universal behavior of δ_1 because a ratio of $\tilde{\varepsilon}_m$ to Δ_m determines the phase shift δ_m , i.e., $\delta_m = \cot^{-1}(\tilde{\varepsilon}_m/\Delta_m)$.

Figures 5(c) and 5(d) show the renormalization factors $Z_m = \tilde{\Delta}_m/\Delta$ and the Wilson ratios $R_{m,m'}$, respectively. As in the $U/(\pi \Delta) = 2.0$ case, the quasiparticle parameters Z_2 and R_{23} for the doubly degenerate states at the Fermi level continuously evolve from the SU(4) value to the SU(2) value as b varies from 0 to ∞ . At zero field, these parameters take the SU(4) values: $Z_{\text{SU}(4)} = 0.25$ and $R_{\text{SU}(4)} - 1 = 0.33$ for $U/(\pi \Delta) = 4.0$. Note that the Wilson ratio is almost saturated to the maximum possible value $R_{\text{SU}(4)}^{\text{max}} - 1 \equiv 1/3$ at zero field. In the opposite limit $b \rightarrow \infty$, these parameters for the twofold degenerate states ($m = 2, 3$) approach those for the symmetric SU(2) Anderson model: $Z_{\text{SU}(2)} \rightarrow 0.026$ and $R_{23}^{\text{SU}(2)} - 1 \rightarrow 0.99$ for the same U . These results show that the strong Coulomb interaction significantly affects the renormalization factor Z_2 or $\tilde{\Delta}_2$. Z_2 determines the energy scale for large field as $T_K^{\text{SU}(2)} = 0.02\Delta$ with Eq. (45). The quasiparticle parameters Z_1 , $R_{1,2}$ and $R_{1,4}$, for the states moving away from the Fermi level approach the noninteracting value in the limit of $b \rightarrow \infty$; i.e., $Z_1 \rightarrow 1$, $R_{1,2} \rightarrow 1$, and $R_{1,4} \rightarrow 1$. Notably, $R_{1,4}$ becomes larger than $R_{1,2}$ for $U/(\pi \Delta) = 4.0$ at finite b . This is quite different what we have found for the smaller interaction case $U/(\pi \Delta) = 2.0$.

In order to clarify this difference, we plot the residual interactions $\tilde{U}_{m,m'}$ as functions of magnetic fields in Figs. 5(e) and 5(f). The magnetic fields of Figs. 5(e) and 5(f) are respectively scaled by $T_K^{\text{SU}(4)}$ and U . In these figures, especially in Fig. 5(f), we can see that $\tilde{U}_{1,4}$ becomes much larger than the other two residual interactions $\tilde{U}_{1,2}$ and $\tilde{U}_{2,3}$ as b increases. This field dependence of $\tilde{U}_{1,4}$ clearly explain why the corresponding Wilson ratio $R_{1,4}$ becomes larger than $R_{1,2}$. We also note that $\tilde{U}_{2,3}$ for the doubly degenerate levels approach the SU(2) symmetric value $\tilde{U}_{2,3}/(\pi \Delta) \rightarrow 0.026$.

All these results discussed in this section indicate that the quantum fluctuations and many-body effects are enhanced for large magnetic fields as the number of active channel decreases from 4 to 2 [36]. We have also shown the enhancement of the fluctuations are more clearly seen for strong interactions by comparing the results for $U/(\pi \Delta) = 4.0$ to those for $U/(\pi \Delta) = 2.0$.

V. TEMPERATURE DEPENDENCE OF MAGNETOCONDUCTANCE

The above discussions about the Fermi-liquid parameters have mainly focused on the zero temperature properties of the

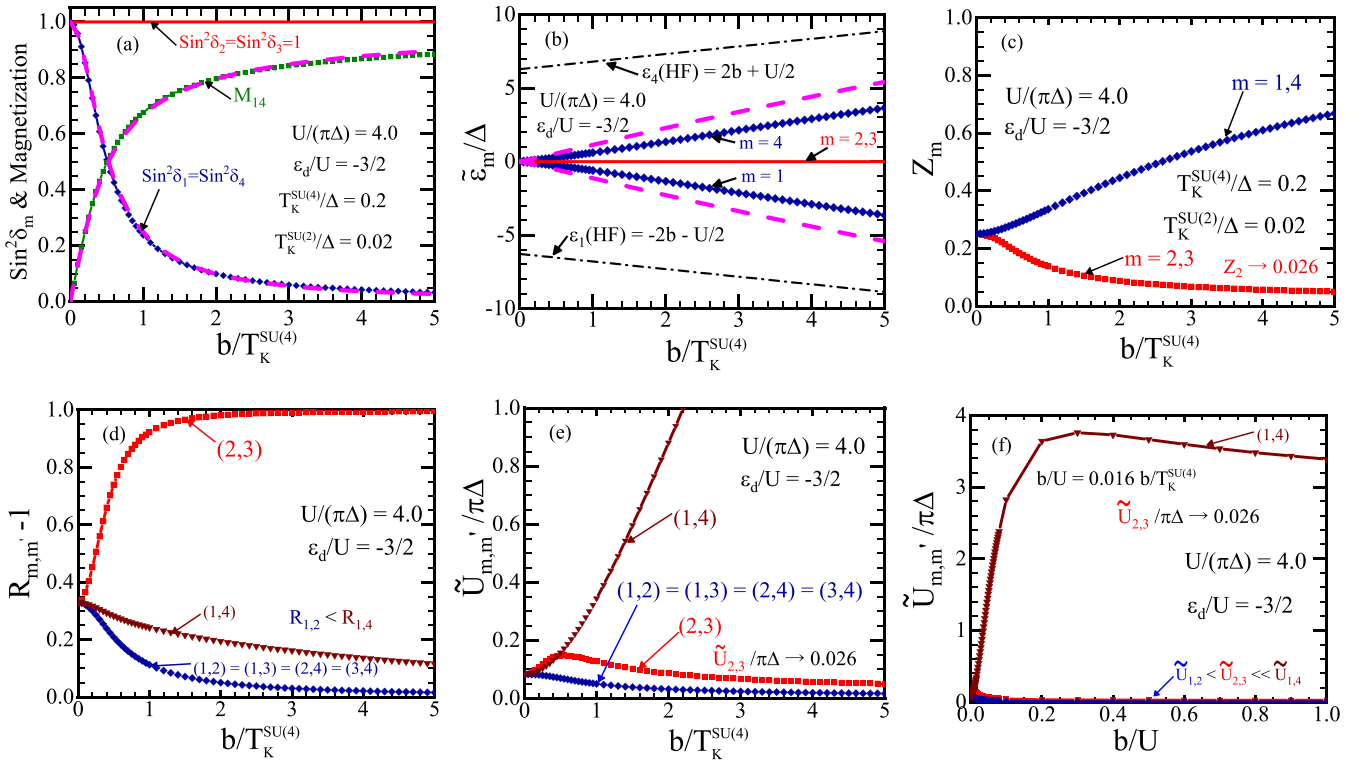


FIG. 5. (a) $\sin^2 \delta_m$ and magnetization $\mathcal{M}_{14} = \langle n_{d1} \rangle - \langle n_{d4} \rangle$, (b) renormalized level position $\tilde{\epsilon}_m$, (c) renormalization factor Z_m , (d) Wilson ratio $R_{m,m} - 1$, and (e) residual interaction $\tilde{U}_{m,m}$ are plotted as functions of magnetic field b at half-filling $\epsilon_d/U = -3/2$ for $U/(\pi\Delta) = 4.0$. The x axis in (a)-(e) is scaled by the SU(4) Kondo temperature $T_K^{\text{SU}(4)} = 0.2\Delta = (0.016U)$ determined at $b = 0$. The axis in (f) is scaled by U for examining the behavior of $\tilde{U}_{m,m}$ at larger magnetic fields. The dot levels ϵ_m are chosen in a such way that is described in Eq. (41). In (a), $\sin^2 \delta_m$ and M_d for $U/(\pi\Delta) = 2.0$ are also plotted by dashed lines to compare them with those for the present case $U/(\pi\Delta) = 4.0$. Similarly, $\tilde{\epsilon}_m$ for $U/(\pi\Delta) = 2.0$ are plotted in (b). The dash-dotted lines indicate the mean-field splitting $\epsilon_1^{\text{HF}} = -(2b + U/2)$ and $\epsilon_4^{\text{HF}} = (2b + U/2)$. In the limit of $b \rightarrow \infty$, $Z_2, R_{2,3} \rightarrow 1$, and $\tilde{U}_{2,3}$ approach the SU(2) values for $U/(\pi\Delta) = 4.0$: $Z_2 \rightarrow 0.026$, $R_{2,3} \rightarrow 1.99$, and $\tilde{U}_{2,3}/\pi\Delta \rightarrow 0.026$.

crossover. The results show that the quasiparticles are strongly renormalized as the ground state undergoes the crossover from the SU(4) Kondo state to the SU(2) Kondo state.

We also study finite temperature properties of the crossover in this section by calculating each component of the magnetoconductance g_m for $m = 1, 2, 3, 4$ and the total conductance g_{tot} . At half-filling, $\epsilon_d = -\frac{3}{2}U$, only two components are independent: $g_2 = g_3$ and $g_1 = g_4$ due to the level structure described in Eq. (41). The finite-temperature conductance, defined in Eq. (23), depends on the excited states whose contributions enter through the spectral function $A_m(\omega, T)$. We calculate the T -dependent $A_m(\omega, T)$, using the NRG with some extended methods for dynamic correlation functions described in Sec. II D and Appendix E, to obtain g_m . We examine two different interactions, $U/(\pi\Delta) = 2.0$ and 4.0 , also for these components of the conductance assuming symmetric couplings $\Delta_L = \Delta_R = \Delta/2$.

A. Conductance for $U/(\pi\Delta) = 2.0$ at half-filling

Figures 6(a)–(d) plot the total conductance g_{tot} and the components $g_2 = g_3$ and $g_1 = g_4$ as functions of the temperature for six values of magnetic fields, $b/T_K^{\text{SU}(4)} = 0.0, 0.25, 0.5, 1.0, 2.0$, and 4.0 . The SU(4) Kondo energy scale, determined at $b = 0$ for $U/(\pi\Delta) = 2.0$, is estimated to be $T_K^{\text{SU}(4)} = 0.41\Delta$ as mentioned in Sec. IV A.

Figure 6(a) shows that the total conductance at $b = 0$ logarithmically increases around $T \sim T_K^{\text{SU}(4)}$. This logarithmic temperature dependence is a hallmark of the SU(4) Kondo effect. g_{tot} increases to the unitary-limit value $4e^2/h$ as temperature goes down to $T \rightarrow 0$. As the magnetic fields increase, the conductance at low-temperatures $T \ll T_K^{\text{SU}(2)}$ decreases from the SU(4) unitary limit value $4e^2/h$ to the SU(2) one $2e^2/h$. We can also see that in a temperature range of $0.1T_K^{\text{SU}(2)} \lesssim T \lesssim T_K^{\text{SU}(4)}$ the conductance curve deforms continuously into the curve for the SU(2) symmetric case. The SU(2) Kondo state emerges for $b \rightarrow \infty$ where the characteristic energy scale becomes $T_K^{\text{SU}(2)} = 0.19\Delta$. Therefore the finite temperature conductance also shows the crossover behavior. To examine how the magnetoconductance g_{tot} evolves with increasing b in more detail, we discuss the two components, g_2 and g_1 .

Figure 6(b) plots the component g_2 which represents contributions of the state $m = 2$ and $m = 3$ remaining at the Fermi level. This component g_2 decreases as b increases in the temperature range of $0.1T_K^{\text{SU}(2)} \lesssim T \lesssim T_K^{\text{SU}(4)}$. In order to investigate the behavior of g_2 in this range in more detail, we introduce an energy scale T_2^* :

$$T_2^* \equiv \frac{\pi}{4} \tilde{\Delta}_2, \quad \tilde{\Delta}_2 = Z_2 \Delta. \quad (57)$$

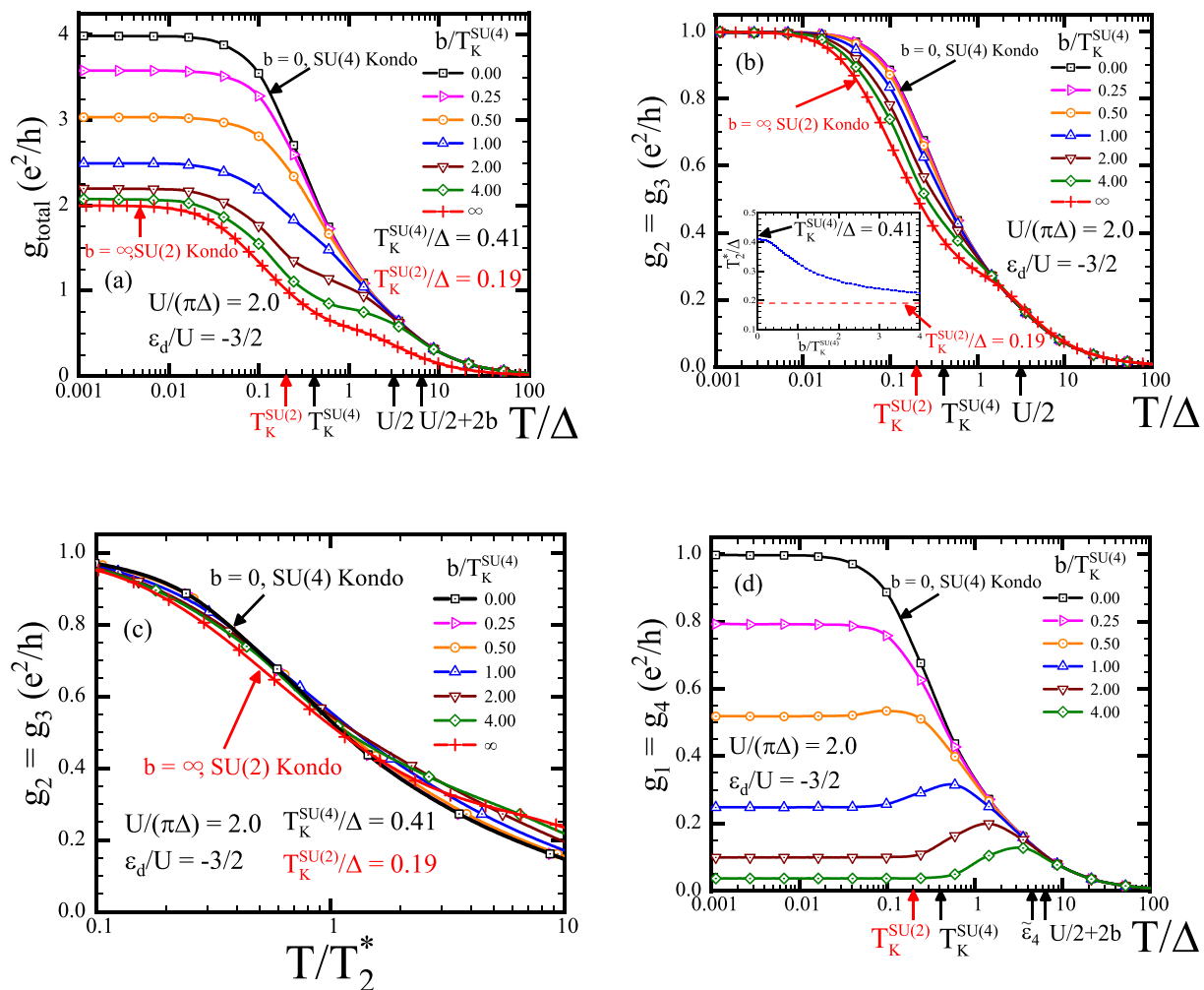


FIG. 6. Temperature dependence of the linear conductance for $U/(\pi\Delta) = 2.0$ are plotted for six values of magnetic fields $b/T_K^{\text{SU}(4)} = 0.0, 0.25, 0.5, 1.0, 2.0,$ and 4.0 at half-filling $\varepsilon_d = -3U/2$. (a) shows the total conductance $g_{\text{tot}} = \sum_{m=1}^4 g_m$. The conductance consists of two components, i.e., $g_2 = g_3$ and $g_1 = g_4$. (b) and (c) show the first one g_2 , and (d) shows the second one g_1 . (a)–(c) also show the results for the SU(2) symmetric case by the symbols (+). In (a), (b), and (d), the x axis is normalized the bare resonance width Δ , and the axis in (c) is normalized by a field dependent energy scale $T_2^* = (\pi/4)Z_2\Delta$. The inset of (b) shows T_2^* as functions of $b/T_K^{\text{SU}(4)}$. At $b = 0$, T_2^* takes the SU(4) symmetric value, $T_K^{\text{SU}(4)}/\Delta = 0.41$. In the opposite limit $b = \infty$, it takes SU(2) value, $T_K^{\text{SU}(2)}/\Delta = 0.19$ which is indicated by the dashed line. The vertical arrows at the bottom of the panels indicate $T_K^{\text{SU}(2)}$, $T_K^{\text{SU}(4)}$, $U/2$, $\tilde{\varepsilon}_4$ and $U/2 + 2b$; specifically the last two, ε_4 and $U/2 + 2b$, are defined with respect to $b/T_K^{\text{SU}(4)} = 4.0$.

Aside from a numerical factor $\pi/4$, this energy T_2^* corresponds to the width $\tilde{\Delta}_2 (= \tilde{\Delta}_3)$ of the Kondo resonance for $m = 2$ and 3 , locked at the Fermi level even at finite magnetic fields. We use this energy scale to examine the scaling behavior. T_2^* coincides with $T_K^{\text{SU}(4)} = 0.41\Delta$ at $b = 0$, and with $T_K^{\text{SU}(2)} = 0.19\Delta$ in the opposite limit $b \rightarrow \infty$. The inset of Fig. 6(b) shows the energy scale T_2^* as functions of b . We can see that T_2^* decreases from $T_K^{\text{SU}(4)}$ to $T_K^{\text{SU}(2)}$ with increasing b . Correspondingly, a region where g_2 shows the $\log T$ dependence moves towards a low temperature side as b increases. Although g_2 decreases with increasing b at the finite temperatures, it approaches the unitary limit e^2/h for $T \rightarrow 0$ for arbitrary magnetic fields. This is because the matching of the spin and orbital Zeeman splitting locks the phase shifts at $\delta_2 = \delta_3 = \pi/2$ even for magnetic fields.

Another important aspect of the crossover is the scaling behavior of the conductance. In Ref. [28], Mantelli and his coworkers examine effects of the spin-orbit interaction on the scaling behavior at quarter filling, $\varepsilon_d = -\frac{1}{2}U$. We examine how the magnetic field affects the scaling at half-filling, $\varepsilon_d = -\frac{3}{2}U$. To explore the scaling behavior, we rescale temperatures by the field dependent energy scale T_2^* defined in Eq. (57) and replot g_2 for the six values of b as functions of the rescaled temperatures T/T_2^* in Fig. 6(c). The six curves are almost overlapped each other in this figure. At low fields $b \lesssim T_K^{\text{SU}(4)}$, the curves remain the same curve as the SU(4) universal one over a wide temperature range. At high fields $b \gg T_K^{\text{SU}(4)}$, the curves collapse into the SU(2) universal curve. At half-filling points $\varepsilon_d = -\frac{N-1}{2}U$, the Wilson ratio determines the T^2 coefficient C_T for the SU(N)

conductance: $C_T = (\pi^2/48)[1 + 2(N-1)(R-1)^2]$. Substituting the Wilson ratio for the SU(4) case $R^{\text{SU}(4)} - 1 = 0.32$ and for the SU(2) case $R^{\text{SU}(2)} - 1 = 0.96$ into the formula of C_T yields the T^2 coefficients C_T of each case for $U/(\pi\Delta) = 2.0$: $C_T^{\text{SU}(4)} \simeq 0.33$ and $C_T^{\text{SU}(2)} \simeq 0.59$. Since $C_T^{\text{SU}(4)} < C_T^{\text{SU}(2)}$, the conductance for $N = 4$ is larger than that for $N = 2$ at the low-temperature regions $T/T_2^* \lesssim 0.1$. Figure 6(c) shows this magnitude relation of the conductance, and thus demonstrates that the scaling behavior depends on the number of orbitals N and the Wilson ratio R .

Figure 6(d) shows the other component $g_1 (= g_4)$ which correspond to the contributions of the other two state moving away from the Fermi level. At low temperatures $T \lesssim T_K^{\text{SU}(4)}$, these components decrease as b increases and eventually vanish at the high magnetic fields $b \gg T_K^{\text{SU}(4)}$. We can also see that g_1 has a peak at large magnetic fields $b \lesssim 0.5T_K^{\text{SU}(4)}$. The emergent peak is caused by thermal excitations from (to) the renormalized level $\tilde{\varepsilon}_1$ ($\tilde{\varepsilon}_4$) which situates deep inside (far above) the Fermi level for large fields as shown in Fig. 5(b). Furthermore, for the large fields, the level structure of the CNT dot approaches the mean-field levels described in Eq. (53), and the atomic-limit peak also emerges at $U/2 + 2b$ (see also Appendix F).

These results obtained for $U/(\pi\Delta) = 2.0$ show a rather moderate evolution of the crossover and the Kondo energy scale T_2^* as $T_K^{\text{SU}(2)}$ is only half of $T_K^{\text{SU}(4)}$.

B. Conductance for $U/(\pi\Delta) = 4.0$ at half-filling

We next examine the conductance for a case of strong interaction $U/(\pi\Delta) = 4.0$ to see more clearly the field-induced crossover at finite temperatures. In this case, the characteristic energy scale for the SU(2) case is significantly suppressed $T_K^{\text{SU}(2)} = 0.02\Delta$, which becomes much smaller than the SU(4) energy scale $T_K^{\text{SU}(4)} = 0.2\Delta$, i.e., the difference is about one order of magnitude.

Figure 7(a) shows that the total conductance g_{tot} for a temperature region $0.1T_K^{\text{SU}(2)} \lesssim T \lesssim T_K^{\text{SU}(4)}$ decreases as magnetic field increases. Since the characteristic energy scale T_2^* defined in Eq. (57) in this case becomes much smaller than that for $U/(\pi\Delta) = 2.0$, the region where the crossover occurs moves towards a low-temperature region, $T \lesssim T_K^{\text{SU}(4)} = 0.2\Delta$. Furthermore, the shoulder structures emerging in the high temperature region are more pronounced.

Figure 7(b) clearly shows that the curves of g_2 evolve from the SU(4) curve to the SU(2) curve during the crossover. Specifically, the energy scale T_2^* around which g_2 shows $\log T$ dependence decreases with increasing magnetic field. The inset of Fig. 6(b) shows the suppression of T_2^* : it decreases from $T_K^{\text{SU}(4)} = 0.2\Delta$ to $T_K^{\text{SU}(2)} = 0.02\Delta$.

The scaling behavior of g_2 in Fig. 6(c) also becomes clear because of this suppression. In a wide range of temperatures, we can see that the scaled results collapse into two different universal curves, i.e., the SU(4) curve for small fields $b/T_K^{\text{SU}(4)} \lesssim 0.25$, and SU(2) curve for large fields $b/T_K^{\text{SU}(4)} \gtrsim 1$. Since the Wilson ratios for $N = 4$ and 2 are respectively saturated to the maximum possible values $R_{\text{SU}(4)}^{\text{max}} - 1 = 1/3$ and $R_{\text{SU}(2)}^{\text{max}} - 1 = 1$, the T^2 coefficients C_T for each N are also saturated: $C_T^{\text{SU}(4)} \simeq 0.34$ and $C_T^{\text{SU}(2)} \simeq 0.62$. Figure 6(c)

clearly shows that g_2 for $b = 0$ is larger than that for $b \rightarrow \infty$ at $T < T_2^*$ because of $C_T^{\text{SU}(4)} < C_T^{\text{SU}(2)}$.

Furthermore, we can recognize that a broad peak emerges for $b \gg T_K^{\text{SU}(4)}$ at $T \approx U/2$. It corresponds to an thermal energy needed to add an electron or a hole to the degenerate states. Thus this atomic limit peak and the quasiparticle excitation peak in Fig. 7(d) at $T \approx 2b + U/2$ yield the shoulder structure of g_{tot} at the high temperatures, as shown in Fig. 7(a).

VI. SPECTRAL PROPERTIES ALONG THE FIELD-INDUCED CROSSOVER

Spectral functions at finite magnetic fields also reflect the crossover from the SU(4) to SU(2) Kondo states. In addition to the Kondo resonance near the Fermi level, the Zeemann splitting causes a shift of the atomic-limit peak to $\pm(2b + U/2)$. The spectral functions for the doubly degenerate states remain the same $A_2(\omega, T) = A_3(\omega, T)$ for finite magnetic fields owing to the dot level structure given in Eq. (41). Following relations additionally hold in the particle-hole symmetric case $\varepsilon_d = -(3/2)U$,

$$A_2(\omega, T) = A_2(-\omega, T), \quad A_1(\omega, T) = A_4(-\omega, T). \quad (58)$$

The second relation shows that A_4 is a mirror image of A_1 , and we discuss A_1 and A_2 in the following. We examine the spectral functions at $T = 0$, and hence we drop the second argument of the functions, namely, $A_m(\omega) \equiv A_m(\omega, T = 0)$, ($m = 1, 2, 3, 4$). As in the previous sections, we consider the two cases for the interaction: (i) $U/(\pi\Delta) = 2.0$ and (ii) $U/(\pi\Delta) = 4.0$. The spectral function obtained by the NRG procedure is a set of discrete δ functions. To obtain a continuous spectrum, the logarithmic Gaussian function is used (see Appendix E 3).

A. Spectral function for $U/(\pi\Delta) = 2.0$

Figure 8(a) shows the total spectral function $A_{\text{tot}}(\omega) = \sum_{m=1}^4 A_m(\omega)$ for five different values of magnetic fields and $U/(\pi\Delta) = 2.0$. At zero magnetic field, we can see that a single SU(4) Kondo resonance peak emerges on the Fermi level $\omega = 0$. As the magnetic field increases in the range of $0 < b < \infty$, the height of the Kondo peak decreases from 4 to 2 in units of $\pi\Delta$ since the resonance peak positions for $m = 1$ and 4 move away from the Fermi level, leaving the other positions for $m = 2$ and 3 just on the Fermi level, as shown in Fig. 4(a). This field dependence of the peak positions results in deforming the peak shape of the SU(4) Kondo resonance into that of the SU(2) Kondo resonance on the Fermi level. Furthermore, two sub peaks emerge at higher energies, i.e., $\pm(2b + U/2)$.

Figure 8(b) plots $A_2 (= A_3)$ for four values of b . $A_2 (= A_3)$ shows such deformation of the peak shape. The deformation of A_2 is not so clear in the case of $U/(\pi\Delta) = 2.0$ since $T_K^{\text{SU}(2)}$ is only half as large as $T_K^{\text{SU}(4)}$. Nevertheless, the inset of Fig. 8(b) which is an enlarged view around the Fermi level shows that the resonance width on the Fermi level becomes sharper. The sharpening of the width leads to the decrease of the spectral weight. As the magnetic field increases, A_2 also develops two sub peaks at $\omega = \pm U/2$ to compensate the decrease of the weight. The two peak positions correspond to

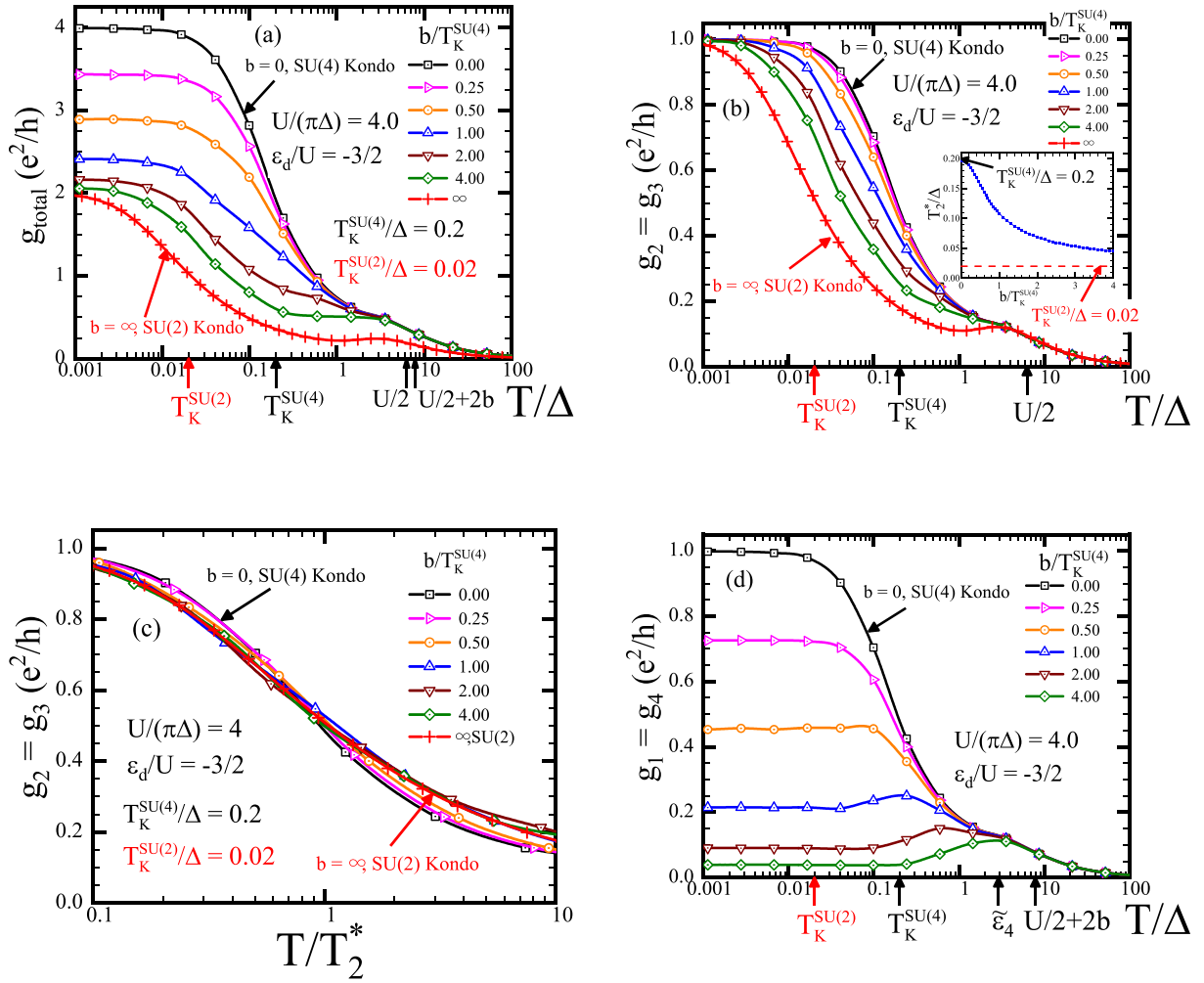


FIG. 7. Temperature dependence of the linear conductance for $U/(\pi\Delta) = 4.0$ are plotted for six values of magnetic fields $b/T_K^{\text{SU}(4)} = 0.0, 0.25, 0.5, 1.0, 2.0, 4.0$ at half-filling $\varepsilon_d = -3U/2$. (a) shows the total conductance $g_{\text{tot}} = \sum_{m=1}^4 g_m$. The conductance consists of two components, i.e., $g_2 = g_3$ and $g_1 = g_4$. (b) and (c) show the first one g_2 , and (d) shows the second one g_1 . (a)–(c) also show the results for the SU(2) symmetric case by the symbols (+). In (a), (b), and (d), the x axis is normalized the bare resonance width Δ , and the axis in (c) is normalized by characteristic energy scales T_2^* . The inset of (b) shows T_2^* as functions of $b/T_K^{\text{SU}(4)}$. At $b = 0$, T_2^* takes the SU(4) symmetric value, $T_K^{\text{SU}(4)}/\Delta = 0.20$. In the opposite limit $b = \infty$, it takes SU(2) value, $T_K^{\text{SU}(2)}/\Delta = 0.02$ which is indicated by the dashed line. The vertical arrows at the bottom of the panels indicate $T_K^{\text{SU}(2)}$, $T_K^{\text{SU}(4)}$, $U/2$, $\tilde{\varepsilon}_4$, and $U/2 + 2b$; specifically the last two, $\tilde{\varepsilon}_4$ and $U/2 + 2b$, are defined with respect to $b/T_K^{\text{SU}(4)} = 4.0$.

the excitation energies on adding an electron or hole to the dot. In Appendix F, we provide analytic expressions of the spectral functions in the atomic limit $v_v \rightarrow 0$, where the CNT dot is disconnected from the metallic leads. The remaining degenerate states turn into the SU(2) Kondo state in the limit of $b \rightarrow \infty$, indicating that the states undergo the crossover from the SU(4) to SU(2) Kondo state.

Figure 8(c) shows the other component $A_1(\omega)$, which corresponds to the component of the level going down from the Fermi level. Note that $A_4(\omega) = A_1(-\omega)$, as mentioned. We can see that the spectral weight transfers to the negative frequency region $\omega < 0$, and an evolution of its resonance peak position shows good agreement with the field dependence of $\tilde{\varepsilon}_1$ presented in Fig. 4(a). This transfer leads to the development of the sub peaks and decrease of the Kondo peak of A_{tot} . With increasing magnetic fields, the resonance peak at $\omega = \tilde{\varepsilon}_1$ merges with the atomic-limit peak at $\omega = -U/2 - 2b$,

which shifts from the zero field position $-U/2$ in the presence of b . This shift of the atomic-limit peak, which we discuss in the Appendix F, results from the descent of the energy level ε_1 described in Eq. (41). For much larger fields $b \gg T_K^{\text{SU}(4)}$, the curve of A_1 approaches the Lorentzian form. Therefore the quasiparticle state of $m = 1$ is unrenormalized from the correlated Kondo state to the bare state.

B. Spectral function for $U/(\pi\Delta) = 4.0$

In order to investigate the effects of the strong interaction on the spectral functions, we next discuss the spectral functions for $U/(\pi\Delta) = 4.0$. Figures 9(a)–9(c) respectively show results of A_{tot} , A_2 , and A_1 . We compare these results with the corresponding results for the weak interaction case in Fig. 8, A_{tot} for the strong interaction in Fig. 9(a) shows a similar trend as that for $U/(\pi\Delta) = 2.0$ in Fig. 8(a). However,

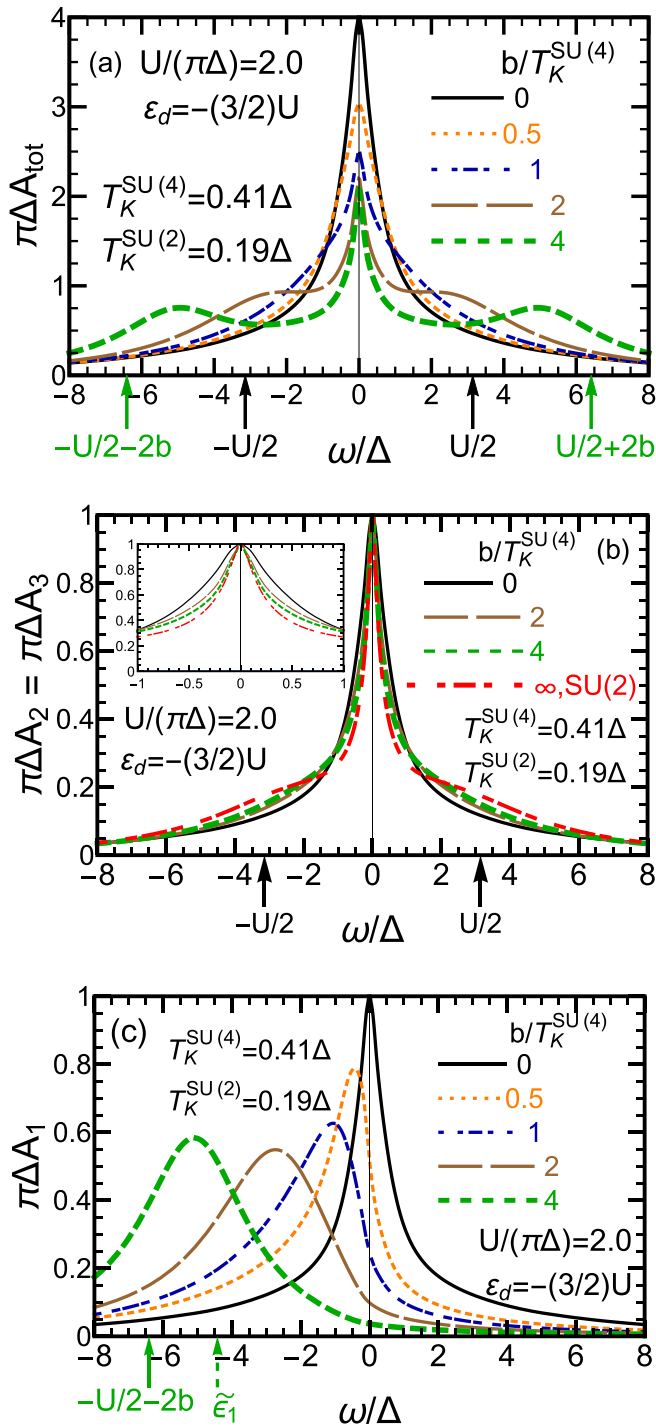


FIG. 8. Zero temperature spectral functions for $U/(\pi\Delta) = 2.0$ are plotted for five values of magnetic fields, $b/T_K^{\text{SU}(4)} = 0.0, 0.5, 1.0, 2.0, 4.0$ at half-filling $\varepsilon_d = -3U/2$: (a) $A_{\text{tot}}(\omega) = \sum_{m=1}^4 A_m(\omega)$, (b) $A_2(\omega)$, and (c) $A_1(\omega)$. Vertical arrows at the bottom of the panels indicate the points $\omega = \pm U/2$ and $\omega = \pm(2b + U/2)$ where peaks emerge in the atomic limit. The peaks of $\omega = \pm(2b + U/2)$ are for the largest value of b among the five, $b/T_K^{\text{SU}(4)} = 4.0$. The position of the renormalized resonance level $\tilde{\varepsilon}_1$ for the same value of b are also shown in the bottom.

the width of resonance for $U/(\pi\Delta) = 4.0$ is smaller than that for $U/(\pi\Delta) = 2.0$ in arbitrary magnetic fields, because U is larger.

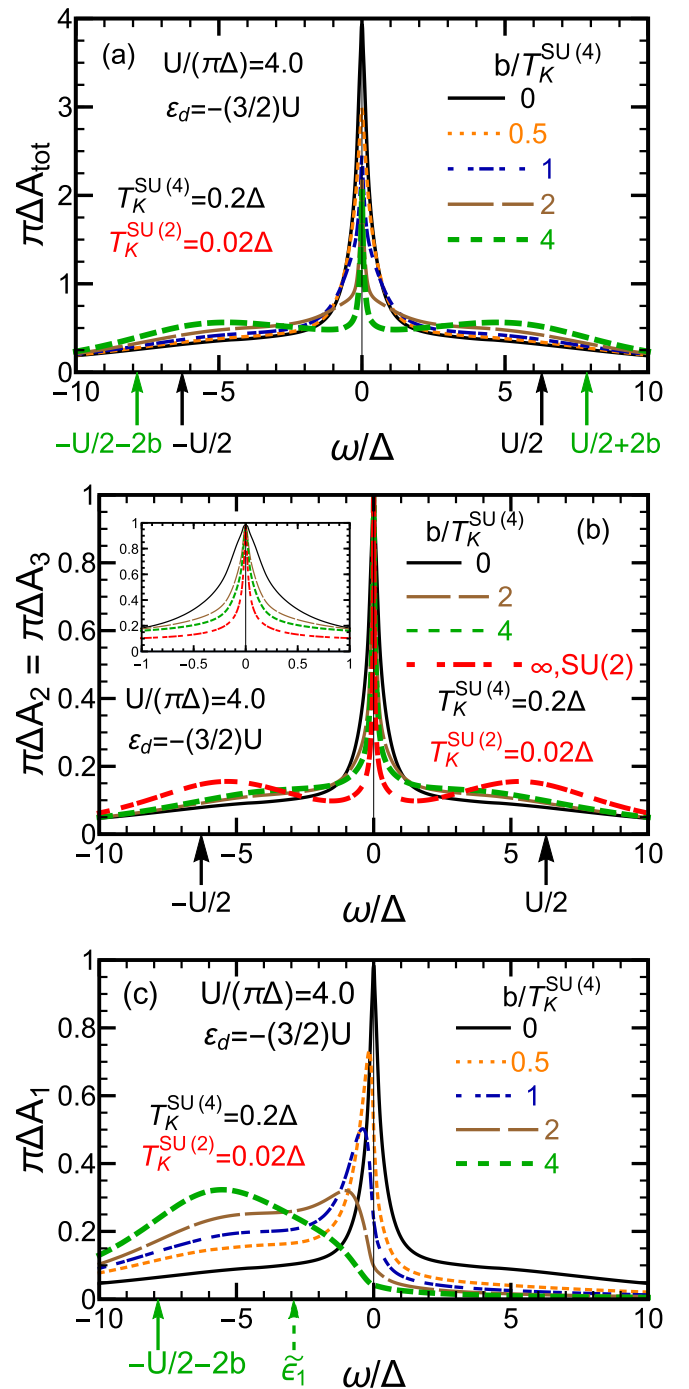


FIG. 9. Spectral functions for $U/(\pi\Delta) = 4.0$ are plotted for five values of magnetic fields, $b/T_K^{\text{SU}(4)} = 0.0, 0.5, 1.0, 2.0, 4.0$ at half-filling $\varepsilon_d = -3U/2$: (a) $A_{\text{tot}}(\omega) = \sum_{m=1}^4 A_m(\omega)$, (b) $A_2(\omega)$, and (c) $A_1(\omega)$. Vertical arrows at the bottom of the panels indicate the points $\omega = \pm U/2$ and $\omega = \pm(2b + U/2)$ where peaks emerge in the atomic limit. The peaks of $\omega = \pm(2b + U/2)$ are for the largest value of b among the five, $b/T_K^{\text{SU}(4)} = 4.0$. The position of the renormalized resonance level $\tilde{\varepsilon}_1$ for the same value of b are also shown in the bottom.

The component A_2 in Fig. 9(b) more clearly shows the narrowing of the resonance width than that for $U/(\pi\Delta) = 2.0$, because $T_K^{\text{SU}(2)}$ is smaller than $T_K^{\text{SU}(4)}$ by one order of magnitude in this case i.e., $T_K^{\text{SU}(2)} = 0.02\Delta$ and $T_K^{\text{SU}(4)} = 0.2\Delta$.

The narrowing of the width leads to a loss of the spectral weight around the Fermi level, which is compensated by an enhancement of the atomic-limit peak at $\pm U/2$.

The atomic limit peak around $-U/2 - 2b$ of A_1 is broader in the strong interaction case shown in Fig. 9(c) than in the weak interaction case, because the quasiparticle resonance position $\tilde{\varepsilon}_1$ presented in Fig. 5(b) still remains around the Fermi level at the higher fields, $b \gg T_K^{\text{SU}(4)}$. Owing to this remaining, the quasiparticle state is still renormalized even at the higher fields, and thus the shape of A_1 differs from the Lorentzian form.

VII. SUMMARY

We have studied the Kondo effect in a carbon nanotube quantum dot in a wide range of temperature and magnetic field using the numerical renormalization group.

In the first half of the present paper, we have studied finite temperature properties of the SU(4) Kondo state by calculating the finite temperature conductance in a wide range of electron filling N_d . The NRG results nicely agree with the experimental results in the wide range, supporting an emergence of the SU(4) Kondo resonance at low-temperatures, $T \lesssim T_K^{\text{SU}(4)}$. Furthermore, we have precisely examined the temperature dependence of conductance especially at two fixed values of N_d : quarter-filling $N_d = 1$ and half-filling $N_d = 2$. The obtained results show that the scaled conductance of $N_d = 1$ is larger than that of $N_d = 2$ at the low temperatures. A microscopic Fermi-liquid theory, which is extended to arbitrary N_d , successfully explains such different behavior of the conductance depending on N_d . The theory shows that a T^2 coefficient C_T for the conductance vanishes at $N_d = 1$. In contrast to the quarter-filling case, C_T does not become zero at half-filling, but saturates to a strong coupling limit value. Thus the universality depends on the electron filling. We expect that this filling dependence of the universality can be observed.

In the second half of the present paper, we have investigated how magnetic fields affect the ground state and also excited states in the course of the SU(4) to SU(2) Kondo crossover. Our previous papers show that quasiparticle states remaining the Fermi level are renormalized as the number of active levels decreases from four to two. The other two states become unrenormalized in the course of the crossover. The present paper has shown that the renormalization of the quasiparticle states more clearly appear in a strong interaction case because a characteristic energy scale T_2^* clearly decreases from the SU(4) Kondo energy scale $T_K^{\text{SU}(4)}$ to the SU(2) Kondo energy scale $T_K^{\text{SU}(2)}$.

The finite temperature conductance in the magnetic fields also shows such decrease of the energy scale. In addition, the scaling behavior at half-filling shows that the excited states undergo the crossover. Specifically, as soon as the magnetic fields b become comparable to $T_K^{\text{SU}(4)}$, the SU(4) universality is lost, and for the much larger fields, $b \gg T_K^{\text{SU}(4)}$, the SU(2) universality emerges. Furthermore, the NRG results for both SU(2) and SU(4) symmetric cases indicate that the Wilson ratio and the Kondo energy scale determine the low-temperature behavior of half-filled quantum dots.

We have also calculated total spectral function and their components in magnetic fields. The obtained spectral function shows that the resonance states remaining on the Fermi level become sharper as the magnetic field increases, showing a good agreement with the field dependence of the corresponding renormalized resonance width. Furthermore, a spectral weight of the other two states transfers towards the higher frequency region, because the Zeeman splitting shifts the two peak positions upward and downward from the Fermi level. Such transfer results in the emergence of two sub-peaks whose positions approach atomic-limit peak positions.

An interesting future work is to explore how the thermoelectric transport of multilevel quantum dots depends on the electron filling [42,67,68]. We have already had the low-temperature expansions for the thermal conductance [34], and the progress along this line will be discussed elsewhere.

ACKNOWLEDGMENTS

This work was supported by Grant-in-Aid for JSPS Fellows Grant No. JP18J10205 and JSPS KAKENHI Grant Nos. JP18K03495, JP19H00656, JP19H05826, JP16K17723, and JP19K14630, JST CREST Grant No. JPMJCR1876, the French program Agence nationale de la Recherche DYMESYS (ANR2011-IS04-001-01), and Agence nationale de la Recherche MASH (ANR-12-BS04-0016).

APPENDIX A: SYMMETRIES OF HAMILTONIAN

In the case where the impurity level is degenerate $\epsilon_m \equiv \epsilon_d$, the Hamiltonian \mathcal{H} defined in Eq. (1) has the SU(N) symmetry. This is also owing to the fact that the tunneling matrix element and the Coulomb interaction do not depend on the flavour m . It can also be confirmed that \mathcal{H} commutes with each component of the SU(N) generators:

$$\mathbf{J}^\mu \equiv \frac{1}{2} \sum_{m,m'=1}^N \left[d_m^\dagger \boldsymbol{\lambda}_{m,m'}^\mu d_{m'} + \sum_{v=L,R} \int_{-D}^D d\varepsilon c_{v,\varepsilon,m}^\dagger \boldsymbol{\lambda}_{m,m'}^\mu c_{v,\varepsilon,m} \right]. \quad (\text{A1})$$

Here, $\boldsymbol{\lambda}^\mu$ for $\mu = 1, 2, \dots, N^2 - 1$ are the Gell-mann matrices that satisfy the commutation relations,

$$[\boldsymbol{\lambda}^i, \boldsymbol{\lambda}^j] = 2i \sum_{k=1}^{N^2-1} f^{ijk} \boldsymbol{\lambda}^k, \quad (\text{A2})$$

with f^{ijk} the structure factor. The Hamiltonian \mathcal{H} has also an $U(1)_{\text{tot}}$ symmetry and commutes with the total number operator $Q_{\text{tot}} = \sum_{m=1}^N Q_m$. Here, Q_m is the number operator for flavour m :

$$Q_m = \left[n_{dm} + \sum_{v=L,R} \int_{-D}^D d\varepsilon c_{v,\varepsilon,m}^\dagger c_{v,\varepsilon,m} \right], \quad (\text{A3})$$

for $m = 1, 2, \dots, N$. Perturbations that lift the degeneracy of the impurity level lower the symmetry from SU(N) \otimes $U(1)_{\text{tot}}$ to $U(1)_{m=1} \otimes U(1)_{m=2} \otimes U(1)_{m=3} \otimes U(1)_{m=4}$ as \mathcal{H} still commutes with each number operator Q_m .

For carbon nanotube dots, the two states of $m = 2$ and 3 remain degenerated even in magnetic fields when the matching

condition Eq. (40) holds. In the condition, \mathcal{H} commutes with the SU(2)-pseudospin operator,

$$S^\mu \equiv \frac{1}{2} \sum_{m,m'=\uparrow,\downarrow} \left[d_m^\dagger \sigma_{m,m'}^\mu d_{m'} + \sum_{v=L,R} \int_{-D}^D d\varepsilon c_{v,\varepsilon,m}^\dagger \sigma_{m,m'}^\mu c_{v,\varepsilon,m} \right] \quad (\text{A4})$$

acting on the two states. Here, σ^μ for $\mu = x, y$, and z are the Pauli matrices. The pseudospins \uparrow and \downarrow respectively denote the state of $m = 2$ and 3 . Thus the Hamiltonian has the $U(1)_{m=1} \otimes [SU(2) \otimes U(1)]_{m=2,3} \otimes U(1)_{m=4}$ symmetries. The SU(2) symmetry plays a central role in the field-induced SU(4) to SU(2) Kondo crossover.

At half-filling point $\epsilon_d/U = -3/2$, the Hamiltonian \mathcal{H} is invariant under an extended electron-hole transformation:

$$d_1^\dagger \Rightarrow h_4, \quad d_2^\dagger \Rightarrow h_3, \quad d_3^\dagger \Rightarrow h_2, \quad d_4^\dagger \Rightarrow h_1, \quad (\text{A5})$$

and correspondingly, $c_{v,\varepsilon,m}^\dagger \Rightarrow -f_{v,-\varepsilon_{m'},m'}$ for $(m, m') = (1, 4), (2, 3), (3, 2), (4, 1)$. Here, h_m and $f_{v,\varepsilon_{m'},m'}$ annihilate hole in the dot and the conduction bands, respectively.

APPENDIX B: OVERVIEW OF NRG ITERATIONS

We provide a brief overview of an NRG iteration. The NRG Hamiltonian \mathcal{H} for an Anderson impurity model is a semi-infinite tight-binding chain with the impurity at a left end. Specifically,

$$\mathcal{H}_{\text{NRG}} = \mathcal{H}_d^0 + \mathcal{H}_U + \mathcal{H}_{\text{chain}} + \mathcal{H}_T, \quad (\text{B1})$$

$$\mathcal{H}_d^0 = \sum_{m=1}^N \epsilon_m d_m^\dagger d_m, \quad \mathcal{H}_U = U \sum_{m < m'} n_{dm} n_{dm'}, \quad (\text{B2})$$

$$\mathcal{H}_{\text{chain}} = \sum_{n=0}^{\infty} \sum_{m=1}^N t_n (f_{n,m}^\dagger f_{n+1,m} + \text{H.c.}), \quad (\text{B3})$$

$$\mathcal{H}_T = V \sum_{m=1}^N (d_m^\dagger f_{m,0} + \text{H.c.}). \quad (\text{B4})$$

Here, Λ is a logarithmic discretization parameter. A hybridization matrix element V couples the impurity site to a 0th site of the chain. Similarly, a hopping element t_n couples the n th site to $(n+1)$ th site. The explicit forms of V and t_n are respectively

$$\frac{V}{D} = \sqrt{\frac{2\Delta A_\Lambda}{\pi D}}, \quad (\text{B5})$$

$$\frac{t_n}{D} = \frac{(1 + \Lambda^{-1})(1 - \Lambda^{-n-1})}{2(1 - \Lambda^{-2n-1})^{1/2}(1 - \Lambda^{-2n-3})^{1/2}} \Lambda^{-n/2}. \quad (\text{B6})$$

Note that the logarithmic discretization corrects the tunneling matrix element V . A_Λ represents such a correction and can be expressed as

$$A_\Lambda = \frac{1}{2} \left(\frac{1 + 1/\Lambda}{1 - 1/\Lambda} \right) \ln \Lambda. \quad (\text{B7})$$

This correction A_Λ approaches 1 in the continuum limit,

$$\lim_{\Lambda \rightarrow 1} A_\Lambda = 1. \quad (\text{B8})$$

The hopping element t_n exponentially decays with increasing n and its asymptotic form is

$$\frac{t_n}{D} \sim \frac{1 + \Lambda^{-1}}{2} \Lambda^{-n/2}. \quad (\text{B9})$$

To iteratively diagonalize the Hamiltonian \mathcal{H}_{NRG} , we introduce a Hamiltonian \mathcal{H}^L which describe the chain ends at an L th site. The explicit form of \mathcal{H}^L is

$$\mathcal{H}^L = \Lambda^{(L-1)/2} [\mathcal{H}_d^0 + \mathcal{H}_U + \mathcal{H}_{\text{chain}}^L + \mathcal{H}_T], \quad (\text{B10})$$

$$\mathcal{H}_{\text{chain}}^L = \sum_{n=0}^{L-1} \sum_{m=1}^N t_n (f_{n,m}^\dagger f_{n+1,m} + \text{H.c.}). \quad (\text{B11})$$

$\Lambda^{(L-1)/2}$ is multiplied to the right-hand side of Eq. (B10) to makes the hopping element $\Lambda^{(L-1)/2} t_{L-1}$ be order of 1. Eigenvalues of \mathcal{H}^L also become order of 1 due to the multiplication. The full Hamiltonian \mathcal{H}_{NRG} is recovered as the limit of

$$\mathcal{H}_{\text{NRG}} = \lim_{L \rightarrow \infty} \Lambda^{-(L-1)/2} \mathcal{H}^L. \quad (\text{B12})$$

Here, the prefactor corresponds to the energy scale of low-lying excited states of \mathcal{H}^L :

$$\frac{T_L}{D} = \Lambda^{-(L-1)/2}. \quad (\text{B13})$$

To run the iteration, we deduce a recurrence relation for \mathcal{H}^L from Eq. (B10),

$$\mathcal{H}^{L+1} = \Lambda^{1/2} \mathcal{H}^L + \Lambda^{L/2} t_L \sum_{m=1}^N (f_{L,m}^\dagger f_{L+1,m} + \text{H.c.}). \quad (\text{B14})$$

Using this relation, we can construct a matrix for \mathcal{H}^{L+1} from eigenvalues and corresponding eigenstates for the Hamiltonian \mathcal{H}^L . The iterative procedure yields the eigenenergies $E_L(\omega)$ at each L th step. we keep only the N_K eigenstates with the lowest energies and discard the higher energy states because a dimension of \mathcal{H}^L increases with increasing L .

Figure 10 plots low-lying eigenenergies of a CNT dot as functions of even L with typical parameters: $\Lambda = 6.0$, $N_K = 4100$, $U/(\pi\Delta) = 4.0$, $\epsilon_d/U = -3/2$, and $b/T_K^{\text{SU}(4)} = 1.0$. Here, the bare resonance width is $\Delta/D = 1/(100\pi)$. The SU(4) temperature $T_K^{\text{SU}(4)}/\Delta = 0.2$ determined at $b = 0$ scales the magnetic field b . In the value of $b/T_K^{\text{SU}(4)} = 1.0$, the Fermi-liquid state of the dot is in the middle of the SU(4) to SU(2) Kondo crossover as shown in Fig. 5(a). Specifically, Fig. 5(a) shows the magnetization M_d is still not saturated to 1 at the value of b . Figure 10 shows that the energies do not depend on L in the region of $L \gtrsim 20$. At the last iteration $L = 30$, the energy scale T_L given in Eq. (B13) is much smaller not only than $T_K^{\text{SU}(4)}$ but also than the SU(2) Kondo temperature $T_K^{\text{SU}(2)}/\Delta = 0.02$: $T_L/\Delta \approx 1.6 \times 10^{-9}$, $T_L/T_K^{\text{SU}(4)} \approx 8.2 \times 10^{-9}$, and $T_L/T_K^{\text{SU}(2)} \approx 1.0 \times 10^{-7}$. The value of $T_K^{\text{SU}(2)}$ is determined at $b \rightarrow \infty$. Therefore the low-lying energy states approach the Fermi-liquid states for L greater than 20.

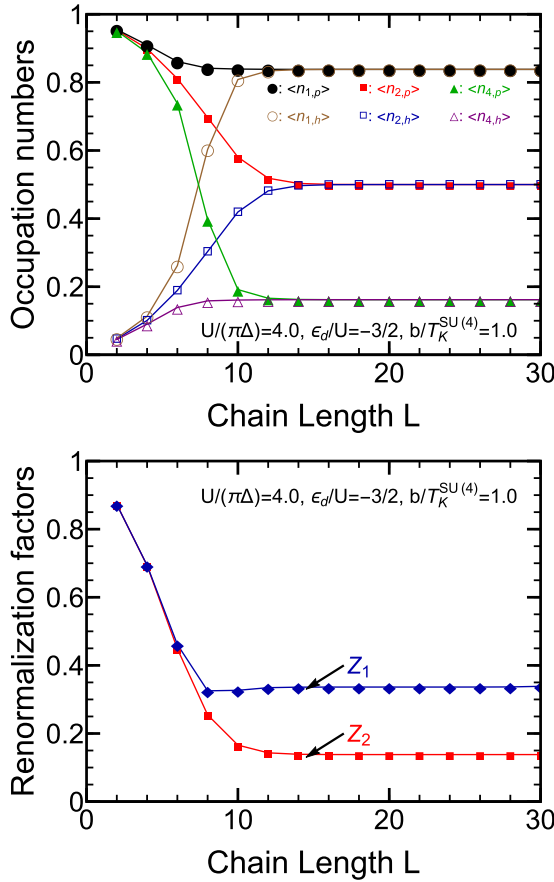


FIG. 11. (a) shows flows of occupation numbers: $\langle n_{1,p} \rangle$, $\langle n_{2,p} \rangle$, $\langle n_{4,p} \rangle$, and $\langle n_{4,h} \rangle$. (b) shows those of renormalization factors: Z_1 and Z_2 . The x axis is the NRG chain length L in each figure. In (a), Following six symbols, \bullet , \circ , \square , \blacktriangle , and \triangle respectively denote the values of $\langle n_{1,p} \rangle$, $\langle n_{1,h} \rangle$, $\langle n_{2,p} \rangle$, $\langle n_{2,h} \rangle$, $\langle n_{4,p} \rangle$, and $\langle n_{4,h} \rangle$. In (b), \bullet and \blacksquare respectively denote the values of Z_1 and Z_2 . The parameters are $U/(\pi\Delta) = 4.0$, $\epsilon_d/U = -3/2$, and $b/T_K^{\text{SU}(4)} = 1.0$ for each figure. These parameters are the same as those for Fig. 10. The SU(4) Kondo temperature is $T_K^{\text{SU}(4)}/\Delta = 0.2$ for the values of U and ϵ_d . Eq. (41) describes the magnetic field b dependence of the four dot levels ϵ_1 , ϵ_2 , ϵ_3 , and ϵ_4 .

$M_d = \langle n_{d,1} \rangle - \langle n_{d,4} \rangle = 0.67$. Figure 5(a) shows this value of M_d at the point of $b/T_K^{\text{SU}(4)} = 1.0$.

Figure 11(b) plots the chain length L dependence of renormalization factors Z_m , which are ratios of Δ_m to Δ , i.e., $Z_m = \tilde{\Delta}_m/\Delta$. We note that the electron-hole symmetry also makes two of the four factors independent: $Z_1 = Z_4$ and $Z_2 = Z_3$. This figure shows that values of Z_1 and Z_2 respectively converge to $Z_1 = 0.34$ and $Z_2 = 0.14$. Since the value of Z_2 is about ten times as large as the SU(2) limit value 0.026, the Fermi-liquid state at $b/T_K^{\text{SU}(4)} = 1.0$ is in the middle of the crossover between the SU(4) and SU(2) Kondo state.

The NRG iteration also yields higher excitation energies from the ground state. $E_{k,p,m}$ and $E_{k,h,m}$ respectively represent such electron and hole excitation energies. We note that $E_{k,p,m} > 0$ and $E_{k,h,m} < 0$. They describe a free quasiparticle Hamiltonian,

$$\mathcal{H}^0 = \sum_{m=1}^N \sum_k (E_{k,p,m} p_{k,m}^\dagger p_{k,m} - E_{k,h,m} h_{k,m}^\dagger h_{k,m}). \quad (\text{C11})$$

Here, operators $p_{k,m}^\dagger$ and $h_{k,m}^\dagger$ respectively create the quasiparticle with $E_{k,p,m}$ and the quasihole with $E_{k,h,m}$. Correspondingly, $p_{k,m}$ and $h_{k,m}$ annihilate the quasiparticle and quasihole. The ground state $|0\rangle$ is defined such that $p_{k,m}|0\rangle = 0$ and $h_{k,m}|0\rangle = 0$. A linear combination of $p_{k,m}^\dagger$ and $h_{k,m}$ expresses the operator d_m^\dagger which creates the impurity electron,

$$d_m^\dagger = \sum_k (p_{k,m}^\dagger \phi_{k,p,m}(-1) + h_{k,m} \phi_{k,h,m}(-1)). \quad (\text{C12})$$

To calculate Wilson ratios $R_{m,m'}$ defined in Eq. (18), we consider a residual interaction term,

$$\mathcal{H}_L^U = \Lambda^{(L-1)/2} \sum_{m < m'} \tilde{U}_{m,m'} N [n_{dm} n_{dm'}]. \quad (\text{C13})$$

Here, $\tilde{U}_{m,m'}$ is the strength of the residual interaction between the quasiparticles. N is the normal ordering operator. We examine how the interaction affects the low-lying many-particle states to a first order perturbation in $\tilde{U}_{m,m'}$. This order calculation accurately describes the effects of the interaction on the low-energy states because the term vanishes in the limit of $L \rightarrow \infty$. For the explicit calculation, we introduce a two-particle excited state from the ground state:

$$|A\rangle = p_{1,m}^\dagger p_{1,m'}^\dagger |0\rangle, \quad (\text{C14})$$

where $m \neq m'$. The NRG iteration calculates a corresponding eigenvalue $E_{pp}(L)$. The first order calculation of $\tilde{U}_{m,m'}$ also gives E_{pp} ,

$$\begin{aligned} E_{pp}(L) &= \langle A | \mathcal{H}^0 + \mathcal{H}_L^U | A \rangle \\ &= 2E_{p,m}(L) + \tilde{U}_{m,m'} \Lambda^{-\frac{L-1}{2}} |\beta_{1,p,m}|^2 |\beta_{1,p,m'}|^2. \end{aligned} \quad (\text{C15})$$

In this equation, $|\beta_{1,p,m}|^2$ is given by

$$|\beta_{1,p,m}|^2 = \frac{\Lambda^{(L-1)/2}}{1 - \tilde{V}_m^2 \Lambda^{(L-1)} \left. \frac{d g_{00,m}(E)}{dE} \right|_{E=E_{1,p,m}}}, \quad (\text{C16})$$

where $\tilde{V}_m^2 = 2D\tilde{\Delta}_m A_\Lambda/\pi$. The L dependent $\tilde{U}_{m,m'}(L)$ is deducible from Eq. (C15) since the NRG iteration procedure determines $E_{pp}(L)$ in the left hand of the equation. We can alternatively consider two hole excitations to calculate $\tilde{U}_{m,m'}$. Considering particle-hole excitations and hole-particle excitations also yields $\tilde{U}_{m,m'}$. Here, the word ‘‘particle-hole excitations’’ denote one particle excitation with m flavour and one hole excitation with m' flavour. The word ‘‘hole-particle excitations’’ similarly denote one hole and one particle excitation with m and m' . Thus $\tilde{U}_{m,m'}$ is calculable by four different ways. $\tilde{U}_{m,m'}^{pp}(L)$, $\tilde{U}_{m,m'}^{hh}(L)$, $\tilde{U}_{m,m'}^{ph}(L)$, and $\tilde{U}_{m,m'}^{hp}(L)$ denote the residual interaction deduced from the two-particle, two-hole, particle-hole and hole-particle excitation energies, respectively.

Figures 12(a)–12(c) respectively plot L dependence of $\tilde{U}_{2,3}$, $\tilde{U}_{1,2}$, and $\tilde{U}_{1,4}$ which are calculated by the four ways. The three figures show that $\tilde{U}_{m,m'}^{pp}$, $\tilde{U}_{m,m'}^{hh}$, $\tilde{U}_{m,m'}^{ph}$, and $\tilde{U}_{m,m'}^{hp}$ converge a same value $\tilde{U}_{m,m'}$ for each (m, m') . Each inset clearly shows such convergence of the four values. The converged values are $\tilde{U}_{2,3}/(\pi\Delta) = 0.13$, $\tilde{U}_{1,2}/(\pi\Delta) = 0.05$, and $\tilde{U}_{1,4}/(\pi\Delta) = 0.35$.

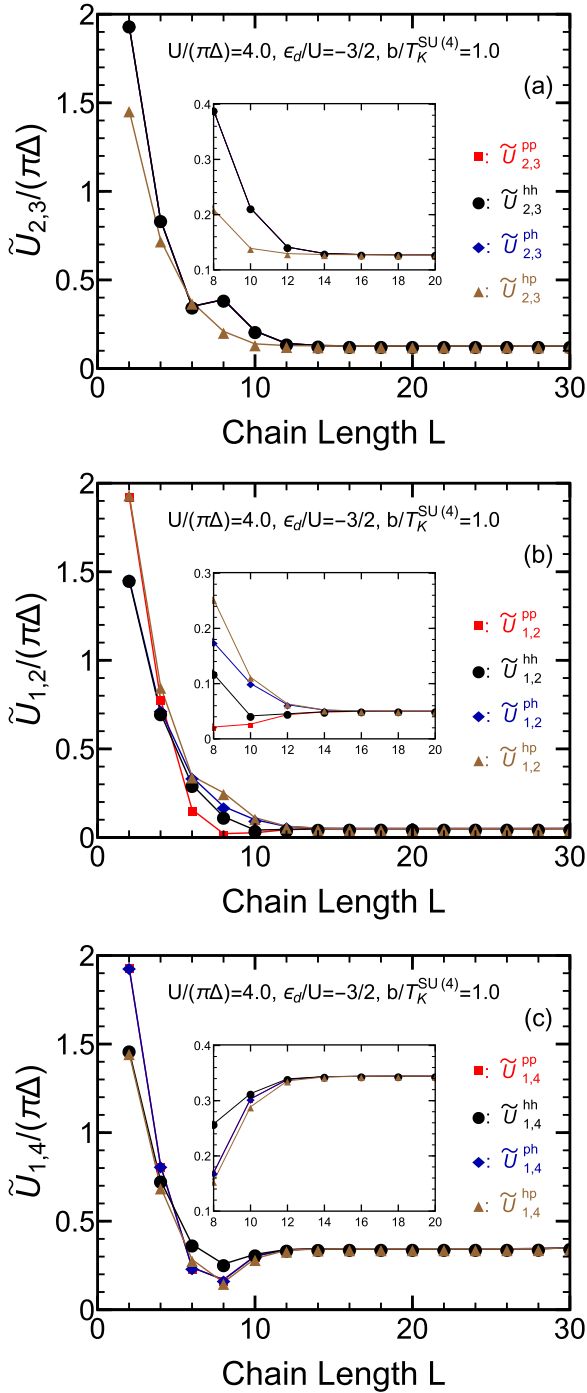


FIG. 12. Residual interactions $\tilde{U}_{m,m'}$ are plotted as functions of the chain length L . (a), (b), and (c) respectively show $(m,m') = (2,3)$, $(1,2)$, and $(1,4)$ element of $\tilde{U}_{m,m'}$. The particle-hole symmetry given by Eq. (A5) imposes following relations to the residual interactions: $\tilde{U}_{1,2} = \tilde{U}_{1,3} = \tilde{U}_{2,4} = \tilde{U}_{3,4}$. The parameters are $U/(\pi\Delta) = 4.0$, $\epsilon_d/U = -3/2$, and $b/T_K^{\text{SU}(4)} = 1.0$ for every three figure. The SU(4) Kondo temperature is $T_K^{\text{SU}(4)}/\Delta = 0.2$ for the values of U and ϵ_d . Following four symbols: \blacksquare , \bullet , \blacklozenge , and \blacktriangle respectively represent $\tilde{U}_{m,m'}^{pp}$, $\tilde{U}_{m,m'}^{hh}$, $\tilde{U}_{m,m'}^{ph}$, and $\tilde{U}_{m,m'}^{hp}$ in each figure. The insets show an enlarged view in the range of $8 \leq L \leq 20$.

The Wilson ratios $R_{m,m'}$ are deducible from the obtained values of $\delta_m = \langle n_{dm} \rangle / \pi$, Z_m , and $\tilde{U}_{m,m'}$ using Eqs. (54)–(56). Figure 13 plots $R_{2,3} - 1$, $R_{1,4} - 1$, and $R_{1,2} - 1$ as func-

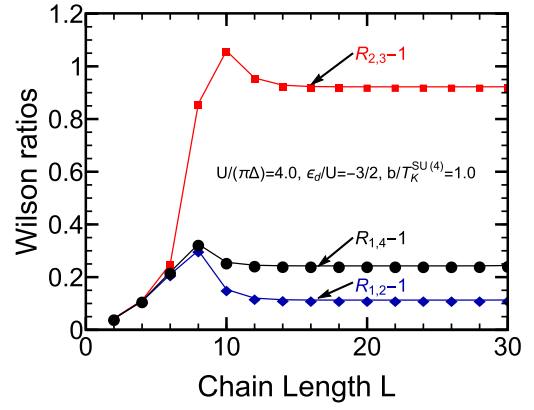


FIG. 13. Wilson ratios $R_{2,3} - 1$, $R_{1,4} - 1$, and $R_{1,2} - 1$ are plotted as functions of the chain length L for the parameters: $U/(\pi\Delta) = 4.0$, $\epsilon_d/U = -3/2$, and $b/T_K^{\text{SU}(4)} = 1.0$. Each three symbol, i.e., \blacksquare , \bullet , and \blacklozenge represents values of $R_{2,3} - 1$, $R_{1,4} - 1$, and $R_{1,2} - 1$, respectively. The SU(4) Kondo temperature is $T_K^{\text{SU}(4)}/\Delta = 0.2$ for the values of U and ϵ_d .

tions of L . The four values of $\tilde{U}_{m,m'}^{pp}$, $\tilde{U}_{m,m'}^{hh}$, $\tilde{U}_{m,m'}^{ph}$, and $\tilde{U}_{m,m'}^{hp}$ are averaged to calculate the ratios $R_{m,m'} - 1$. Each of the three ratios converges for $L \gtrsim 20$. The converged values are $R_{2,3} - 1 = 0.92$, $R_{1,2} - 1 = 0.11$, and $R_{1,4} - 1 = 0.24$. $R_{2,3}$ becomes larger than the other two ratios because the corresponding impurity levels of $R_{2,3}$ remain the Fermi level.

APPENDIX D: FERMI-LIQUID PARAMETERS FOR SINGLE ORBITAL ANDERSON IMPURITY

We briefly discuss how the Fermi liquid state of the single Anderson impurity evolves with increasing magnetic field. The field dependence of the Fermi liquid parameters have been discussed also in Refs. [65,66]. Figures 14(a) and 14(b) plot NRG results of the Fermi liquid parameters and the residual interaction, respectively. In the NRG calculations, the spin-dependent impurity level is chosen such that $\epsilon_{d,\sigma} = \epsilon_d + \text{sgn}(\sigma)b$, and the center of the impurity level is locked at the half-filling, $\epsilon_d = -U/2$. Figure 14(a) shows that the transmission probability $T(0) = \sin^2 \delta$ decreases as soon as magnetic fields become comparable with the Kondo temperature $T_K^{\text{SU}(2)}$, and correspondingly, the induced magnetization is rapidly saturated to 1, i.e., $M_d \rightarrow 1$. In contrast, Z and $R - 1$ vary more slowly than $T(0)$ and M_d with the scales of U . The inset of Fig. 14(a) shows that Δ and $R - 1$ are still renormalized for small magnetic fields $b \lesssim T_K^{\text{SU}(2)}$. For large magnetic fields $b \gg T_K^{\text{SU}(2)}$, these parameters approach the noninteracting values, $Z \rightarrow 1$ and $R - 1 \rightarrow 1$.

The residual interaction plotted in Fig. 14(b) also varies from a zero field value $4T_K^{\text{SU}(2)} = 0.23\pi\Delta$ with increasing b . For small magnetic fields $b \lesssim 0.2U$, \tilde{U} is enhanced and its value becomes larger than the bare Coulomb interaction U . As magnetic fields further increase, it decreases from the enhanced value to the bare value U .

APPENDIX E: NRG FOR DYNAMICAL CORRELATIONS

1. Spectral function and self-energy

In this work, the spectral function $A_m(\omega)$ has been calculated using the “complete Fock-space basis set,” developed by

Andes *et al.* [24,25] and by Weichselbaum and von Delft [26]. In this approach, contributions of the high energy states which are discarded at the NRG steps can be recovered to form a complete basis for the Wilson's NRG chain, by carrying out the backward iteration. The merit of this approach is that the sum rule for the spectral weights can be fulfilled.

We have also employed the method due to Bulla, Hewson, and Pruschke [62]: we have calculated not only $G_m(\omega)$ but also the higher-order Green's function $F_m(\omega)$

$$F_m(\omega) = -i \int_0^\infty dt e^{i(\omega+i0^+)t} \times \sum_{m'(\neq m)} \langle \{n_{dm'}(t) d_m(t), d_m^\dagger(0)\} \rangle. \quad (\text{E1})$$

Then, the self-energy can be determined directly through the relation $\Sigma_m(\omega) = UF_m(\omega)/G_m(\omega)$. The final form of the Green's function has been obtained from $\Sigma_m(\omega)$ and the non-interacting Green's function $G_m^0(\omega)$ using the Dyson equation given in Eq. (7). The merit to treat the self-energy as an input is that the fully analytic expression which is not affected by the logarithmic discretization can be used for $G_m^0(\omega)$.

2. The z averaging

The size of the Hilbert space to be diagonalized at each NRG step increases as the number of conduction electron channels increases. To ensure the accuracy of the NRG calculation, a large Λ is used for quantum impurities with a number of internal degrees of freedom.

Oliveira and Oliveira found that thermodynamic averages which are calculated for large Λ show an artificial oscillation at low temperatures [59,61], and they proposed the z averaging for removing such an artificial oscillation. The parameter z slides a set of discretization points from that of the standard Wilson chain [22],

$$\pm\Lambda^{-n} \rightarrow \pm\Lambda^{-(n+1-z)}, \quad n = 0, 1, 2, \dots, \quad (\text{E2})$$

with $0 \leq z \leq 1$. For $z = 1$, it coincides with the standard Wilson chain. The discretized conduction band can be transformed into a z dependent Wilson chain

$$\mathcal{H}_c \Rightarrow \sum_{n=0}^{\infty} \sum_{m=1}^4 t_n(z) (f_{n,m}^\dagger f_{n+1,m} + f_{n+1,m}^\dagger f_{n,m}). \quad (\text{E3})$$

The hopping matrix element $t_n(z)$ that can be determined using the Householder algorithm summarized in Refs. [59,61]. We have carried out NRG calculations for some fixed values of z , and calculate expectation values using the obtained eigenstates. Then, an average is taken over “ z ” for two different values $z = 0.5$ and 1 , which is enough to eliminate the artificial oscillations in our case.

3. Logarithmic-Gaussian function to broaden discrete spectral function

We have calculated the spectral function A_m using the Lehman representation given in Eq. (F1). The resulting function is a set of discrete δ functions at frequencies ω_n . Replacing the δ function to the logarithmic-Gaussian function makes A_m continuous since the NRG energy scale T_L given

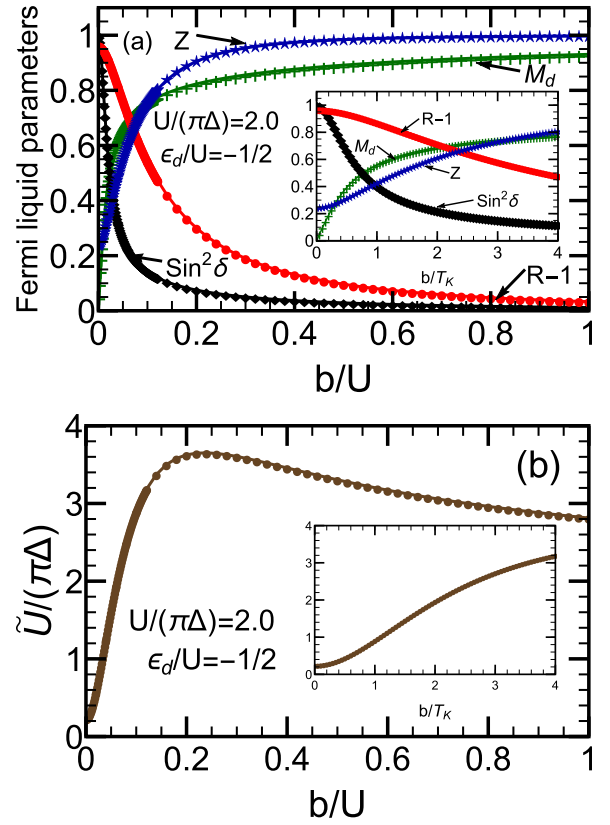


FIG. 14. (a) Magnetic field dependence of Fermi liquid parameters for single orbital Anderson impurity at the electron-hole symmetric point $\epsilon_d/U = -1/2$ for $U/(\pi\Delta) = 2.0$. At this point, a total occupation number is locked at one, i.e., $\langle n_{d\downarrow} \rangle + \langle n_{d\uparrow} \rangle = 1$ at arbitrary magnetic fields, and thus $\langle n_{d\sigma} \rangle$ can be expressed in terms of the magnetization $M_d \equiv \langle n_{d\uparrow} \rangle - \langle n_{d\downarrow} \rangle$ as follows: $\langle n_{d\sigma} \rangle = (1 + \text{sgn}(\sigma)M_d)/2$. Furthermore, $\text{sin}^2 \delta_\uparrow = \text{sin}^2 \delta_\downarrow$ and $Z_\uparrow = Z_\downarrow$. (b) Residual interaction \tilde{U} as a function of b . The x axis is scaled by the Coulomb interaction U . Each inset shows an enlarged view of the region around $b = 0$. In the insets, the axis is scaled by the Kondo temperature $T_K^{\text{SU}(2)} = 0.19\Delta = (0.03U)$.

in Eq. (B13) exponentially falls off with increasing the chain length L . The function to broaden a particle excitation peak at $\omega_n > 0$ is

$$X(\omega) = \frac{e^{-b^2/4}}{b\omega_n\sqrt{\pi}} \exp \left\{ - \left(\frac{\ln(\omega/\omega_n)}{b} \right)^2 \right\}, \quad (\text{E4})$$

which is defined for $\omega > 0$. Correspondingly, a hole excitation peak at $\omega_n < 0$ is broadened by

$$Y(\omega) = \frac{e^{-b^2/4}}{b|\omega_n|\sqrt{\pi}} \exp \left\{ - \left(\frac{\ln|\omega/\omega_n|}{b} \right)^2 \right\}, \quad (\text{E5})$$

for $\omega < 0$. We set a broadening parameter $b = 1.1$ for the spectral functions plotted in Figs. 8 and 9. Note that the spectral weight is conserved because the broadening functions are normalized to 1.

APPENDIX F: SPECTRAL FUNCTION IN ATOMIC LIMIT

We consider the atomic limit in order to show how the spectral weight of the impurity states evolves as magnetic

increases at high energies in the case that the Zeemann splittings of the impurity levels are given by Eq. (41).

At zero temperature, the flavour m -resolved single-particle spectral function can be written in the Lehmann representation as

$$A_m(\omega) = \frac{1}{M} \sum_{i=1}^M \sum_n [|\langle n|d_m^\dagger|\Psi_{\text{GS},i}\rangle|^2 \delta(\omega - (E_n - E_{\text{GS}})) + |\langle n|d_m|\Psi_{\text{GS},i}\rangle|^2 \delta(\omega + (E_n - E_{\text{GS}}))]. \quad (\text{F1})$$

Here, $|n\rangle$ and E_n are the eigenstate and eigenenergy of Hamiltonian \mathcal{H} , respectively. The ground state $|\Psi_{\text{GS},i}\rangle$ with the energy E_{GS} can generally be degenerate, and the summation over i represents an average over M -fold degenerate states.

In the atomic limit, the CNT dot whose eigenenergies are defined in Eq. (41) is disconnected from the leads ($v_\nu = 0$ for $\nu = L, R$), and there remains twofold degeneracy for the ground state at half-filling $\varepsilon_d = -3U/2$,

$$|\Psi_{\text{GS},2}\rangle = d_1^\dagger d_2^\dagger |0\rangle, \quad (\text{F2})$$

$$|\Psi_{\text{GS},3}\rangle = d_1^\dagger d_3^\dagger |0\rangle. \quad (\text{F3})$$

Either of the two one-particle states, $m = 2$ or 3 situated on the Fermi level, is occupied, and the lowest one-particle level with the energy ε_1 is occupied while the highest one with ε_4 is empty. Therefore the ground energy for these two-electron states becomes

$$E_{\text{GS}} = \varepsilon_1 + \varepsilon_2 + U = 2\varepsilon_d - 2b + U. \quad (\text{F4})$$

We next consider a single-particle excitation to add an electron into the level of $m = 4$, and a single-hole excitation to remove the electron occupying the $m = 1$ level,

$$|\Psi_{p4}\rangle = d_4^\dagger |\Psi_{\text{GS},i}\rangle, \quad E_{p4} = 3\varepsilon_d + 3U, \quad (\text{F5})$$

$$|\Psi_{h1}\rangle = d_1 |\Psi_{\text{GS},i}\rangle, \quad E_{h1} = \varepsilon_d. \quad (\text{F6})$$

The excitation energies from the ground state $i = 2$ and 3 to these two states are given by

$$E_{p4} - E_{\text{GS}} = \varepsilon_d + 2b + 2U = 2b + \frac{U}{2}, \quad (\text{F7})$$

$$E_{\text{GS}} - E_{h1} = \varepsilon_d - 2b + U = -2b - \frac{U}{2}. \quad (\text{F8})$$

Therefore the spectral weights of these processes are given by

$$A_4(\omega) = \delta\left(\omega - \left(2b + \frac{U}{2}\right)\right),$$

$$A_1(\omega) = \delta\left(\omega + \left(2b + \frac{U}{2}\right)\right). \quad (\text{F9})$$

These weights shift towards high-energy region from the usual atomic limit position $\pm U/2$. We have observed the corresponding shifts of the spectral weight in the NRG results shown in Fig. 8(c) and 9(c) although these atomic peaks merge with the resonance peak which also moves away from the Fermi level as b increases.

The other single electron (hole) excitation from the ground state $|\Psi_{\text{GS},2}\rangle$ corresponds to an addition of an electron to the level $m = 3$ (annihilation of an electron from $m = 2$). The similar excitations also occur from $|\Psi_{\text{GS},3}\rangle$. The peaks corresponding to these excitations appear at $\omega = \pm U/2$ in the spectral functions for $m = 2$ and 3 ,

$$A_2(\omega) = A_3(\omega) = \frac{1}{2}\delta\left(\omega - \frac{U}{2}\right) + \frac{1}{2}\delta\left(\omega + \frac{U}{2}\right). \quad (\text{F10})$$

These two peaks are equivalent to the Hubbard peaks for the SU(2) symmetric case.

-
- [1] J. Kondo, *Prog. Theor. Phys.* **32**, 37 (1964).
[2] A. C. Hewson, *The Kondo Problem to Heavy Fermions* (Cambridge University Press, Cambridge, UK, 1993).
[3] L. I. Glazman and M. E. Raikh, *JETP Lett.* **47**, 452 (1988).
[4] T. K. Ng and P. A. Lee, *Phys. Rev. Lett.* **61**, 1768 (1988).
[5] D. Goldhaber-Gordon, J. Göres, M. A. Kastner, H. Shtrikman, D. Mahalu, and U. Meirav, *Phys. Rev. Lett.* **81**, 5225 (1998).
[6] W. Van der Wiel, S. De Franceschi, T. Fujisawa, J. Elzerman, S. Tarucha, and L. Kouwenhoven, *Science* **289**, 2105 (2000).
[7] E. A. Laird, F. Kuemmeth, G. A. Steele, K. Grove-Rasmussen, J. Nygård, K. Flensberg, and L. P. Kouwenhoven, *Rev. Mod. Phys.* **87**, 703 (2015).
[8] S. Sasaki, S. De Franceschi, J. M. Elzerman, W. G. van der Wiel, M. Eto, S. Tarucha, and L. P. Kouwenhoven, *Nature (London)* **405**, 764 (2000).
[9] M.-S. Choi, R. López, and R. Aguado, *Phys. Rev. Lett.* **95**, 067204 (2005).
[10] W. Izumida, O. Sakai, and Y. Shimizu, *J. Phys. Soc. Jpn.* **67**, 2444 (1998).
[11] L. Borda, G. Zaránd, W. Hofstetter, B. I. Halperin, and J. von Delft, *Phys. Rev. Lett.* **90**, 026602 (2003).
[12] F. B. Anders, D. E. Logan, M. R. Galpin, and G. Finkelstein, *Phys. Rev. Lett.* **100**, 086809 (2008).
[13] I. Weymann, R. Chirla, P. Trocha, and C. P. Moca, *Phys. Rev. B* **97**, 085404 (2018).
[14] Y. Nishikawa, A. C. Hewson, D. J. G. Crow, and J. Bauer, *Phys. Rev. B* **88**, 245130 (2013).
[15] A. Makarovski, A. Zhukov, J. Liu, and G. Finkelstein, *Phys. Rev. B* **75**, 241407(R) (2007).
[16] A. J. Keller, S. Amasha, I. Weymann, C. P. Moca, I. G. Rau, J. A. Katine, H. Shtrikman, G. Zaránd, and D. Goldhaber-Gordon, *Nat. Phys.* **10**, 145 (2014).
[17] P. Jarillo-Herrero, J. Kong, H. S. J. van der Zant, C. Dekker, L. P. Kouwenhoven, and S. De Franceschi, *Nature (London)* **434**, 484 (2005).
[18] K. J. G. Götze, D. R. Schmid, F. J. Schupp, P. L. Stiller, C. Strunk, and A. K. Hüttel, *Phys. Rev. Lett.* **120**, 246802 (2018).

- [19] M. Ferrier, T. Arakawa, T. Hata, R. Fujiwara, R. Delagrangé, R. Weil, R. Deblock, R. Sakano, A. Oguri, and K. Kobayashi, *Nat. Phys.* **12**, 230 (2016).
- [20] T. Hata, R. Delagrangé, T. Arakawa, S. Lee, R. Deblock, H. Bouchiat, K. Kobayashi, and M. Ferrier, *Phys. Rev. Lett.* **121**, 247703 (2018).
- [21] K. G. Wilson, *Rev. Mod. Phys.* **47**, 773 (1975).
- [22] H. R. Krishna-murthy, J. W. Wilkins, and K. G. Wilson, *Phys. Rev. B* **21**, 1003 (1980).
- [23] H. R. Krishna-murthy, J. W. Wilkins, and K. G. Wilson, *Phys. Rev. B* **21**, 1044 (1980).
- [24] F. B. Anders and A. Schiller, *Phys. Rev. Lett.* **95**, 196801 (2005).
- [25] R. Peters, T. Pruschke, and F. B. Anders, *Phys. Rev. B* **74**, 245114 (2006).
- [26] A. Weichselbaum and J. von Delft, *Phys. Rev. Lett.* **99**, 076402 (2007).
- [27] M. R. Galpin, F. W. Jayatilaka, D. E. Logan, and F. B. Anders, *Phys. Rev. B* **81**, 075437 (2010).
- [28] D. Mantelli, C. P. Moca, G. Zaránd, and M. Grifoni, *Physica E* **77**, 180 (2016).
- [29] P. Roura-Bas, L. Tosi, A. A. Aligia, and K. Hallberg, *Phys. Rev. B* **84**, 073406 (2011).
- [30] C. Mora, P. Vitushinsky, X. Leyronas, A. A. Clerk, and K. Le Hur, *Phys. Rev. B* **80**, 155322 (2009).
- [31] C. Mora, C. P. Moca, J. von Delft, and G. Zaránd, *Phys. Rev. B* **92**, 075120 (2015).
- [32] M. Filippone, C. P. Moca, A. Weichselbaum, J. von Delft, and C. Mora, *Phys. Rev. B* **98**, 075404 (2018).
- [33] A. Oguri and A. C. Hewson, *Phys. Rev. B* **97**, 035435 (2018).
- [34] Y. Teratani, R. Sakano, and A. Oguri, [arXiv:2001.08348](https://arxiv.org/abs/2001.08348).
- [35] M. Ferrier, T. Arakawa, T. Hata, R. Fujiwara, R. Delagrangé, R. Deblock, Y. Teratani, R. Sakano, A. Oguri, and K. Kobayashi, *Phys. Rev. Lett.* **118**, 196803 (2017).
- [36] Y. Teratani, R. Sakano, R. Fujiwara, T. Hata, T. Arakawa, M. Ferrier, K. Kobayashi, and A. Oguri, *J. Phys. Soc. Jpn.* **85**, 094718 (2016).
- [37] D. R. Schmid, S. Smirnov, M. Margańska, A. Dirnacher, P. L. Stiller, M. Grifoni, A. K. Hüttel, and C. Strunk, *Phys. Rev. B* **91**, 155435 (2015).
- [38] V. Lopes, R. A. Padilla, G. B. Martins, and E. V. Anda, *Phys. Rev. B* **95**, 245133 (2017).
- [39] C. A. Büsser and G. B. Martins, *Phys. Rev. B* **75**, 045406 (2007).
- [40] J. S. Lim, M.-S. Choi, M. Y. Choi, R. López, and R. Aguado, *Phys. Rev. B* **74**, 205119 (2006).
- [41] Y. Kleorin and Y. Meir, *Phys. Rev. B* **96**, 045118 (2017).
- [42] P. Roura-Bas, L. Tosi, A. A. Aligia, and P. S. Cornaglia, *Phys. Rev. B* **86**, 165106 (2012).
- [43] D. Krychowski and S. Lipiński, *Eur. Phys. J. B* **91**, 8 (2018).
- [44] D. C. Langreth, *Phys. Rev.* **150**, 516 (1966).
- [45] H. Shiba, *Prog. Theor. Phys.* **54**, 967 (1975).
- [46] A. Yoshimori, *Prog. Theor. Phys.* **55**, 67 (1976).
- [47] A. C. Hewson, *J. Phys.: Condens. Matter* **13**, 10011 (2001).
- [48] A. Hewson, A. Oguri, and D. Meyer, *Eur. Phys. J. B* **40**, 177 (2004).
- [49] R. Landauer, *Philos. Mag.* **21**, 863 (1970).
- [50] Y. Meir and N. S. Wingreen, *Phys. Rev. Lett.* **68**, 2512 (1992).
- [51] S. Hershfield, J. H. Davies, and J. W. Wilkins, *Phys. Rev. B* **46**, 7046 (1992).
- [52] W. Izumida, O. Sakai, and S. Suzuki, *J. Phys. Soc. Jpn.* **70**, 1045 (2001).
- [53] A. Oguri, *Phys. Rev. B* **85**, 155404 (2012).
- [54] Y. Nishikawa, D. J. G. Crow, and A. C. Hewson, *Phys. Rev. B* **82**, 115123 (2010).
- [55] K. M. Stadler, A. K. Mitchell, J. von Delft, and A. Weichselbaum, *Phys. Rev. B* **93**, 235101 (2016).
- [56] P. Nozières, *J. Low Temp. Phys.* **17**, 31 (1974).
- [57] K. Yosida and K. Yamada, *Prog. Theor. Phys. Suppl.* **46**, 244 (1970).
- [58] K. Yamada, *Prog. Theor. Phys.* **53**, 970 (1975).
- [59] W. C. Oliveira and L. N. Oliveira, *Phys. Rev. B* **49**, 11986 (1994).
- [60] T. A. Costi, *Phys. Rev. B* **64**, 241310(R) (2001).
- [61] M. Yoshida, M. A. Whitaker, and L. N. Oliveira, *Phys. Rev. B* **41**, 9403 (1990).
- [62] R. Bulla, A. C. Hewson, and T. Pruschke, *J. Phys.: Condens. Matter* **10**, 8365 (1998).
- [63] W. Izumida, R. Okuyama, and R. Saito, *Phys. Rev. B* **91**, 235442 (2015).
- [64] W. Izumida, R. Okuyama, A. Yamakage, and R. Saito, *Phys. Rev. B* **93**, 195442 (2016).
- [65] A. C. Hewson, J. Bauer, and W. Koller, *Phys. Rev. B* **73**, 045117 (2006).
- [66] J. Bauer and A. C. Hewson, *Phys. Rev. B* **76**, 035119 (2007).
- [67] T. A. Costi, *Phys. Rev. B* **100**, 161106(R) (2019).
- [68] A. Svilans, M. Josefsson, A. M. Burke, S. Fahlvik, C. Thelander, H. Linke, and M. Leijnse, *Phys. Rev. Lett.* **121**, 206801 (2018).